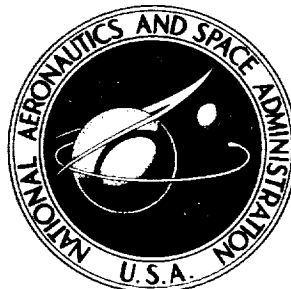


DECLASSIFIED

[REDACTED]

NASA TECHNICAL
MEMORANDUM



UB
NASA TM X-1691

UB
NASA TM X-1691

CASE FILE
COPY

[REDACTED]

CONVECTIVE HEAT TRANSFER
TO THE AMES M2 AND M2-F2
LIFTING ENTRY VEHICLES

*by H. Lee Seegmiller
Ames Research Center
Moffett Field, Calif.*

Declassified by authority of NASA
Classification Change Notices No. 212
Dated ** 31 MAR 1971

[REDACTED]



CONVECTIVE HEAT TRANSFER TO THE AMES M2 AND M2-F2
LIFTING ENTRY VEHICLES

By H. Lee Seegmiller
Ames Research Center
Moffett Field, Calif.

NATIONAL AERONAUTICS AND SPACE ADMINISTRATION

RECEIVED

RECEIVED

RECEIVED

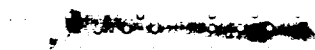
RECEIVED

RECEIVED

RECEIVED

TABLE OF CONTENTS

	<u>Page</u>
SUMMARY	1
INTRODUCTION	1
SYMBOLS	2
EXPERIMENT	3
Test Facilities	3
Test Models and Instrumentation	4
Data Reduction	5
RESULTS AND DISCUSSION	7
Entry Trajectories	7
Body Test Results	8
M2 Dual Pitch Controls	11
M2-F2 Single Pitch Control	12
Fin, Rudder, and Canopy Heating	15
M2-F2 Temperature Visualization Results	15
CONCLUDING REMARKS	16
REFERENCES	18
FIGURES	21



CONVECTIVE HEAT TRANSFER TO THE AMES M2 AND M2-F2

LIFTING ENTRY VEHICLES*

By H. Lee Seegmiller

Ames Research Center

SUMMARY

The convective heat transfer to the Ames M2 and M2-F2 lifting entry vehicles has been measured at angles of attack from -7° to $+77^\circ$ during tests at hypersonic Mach numbers. Transient temperature heating data were obtained at a Mach number, M_∞ , of 10, total enthalpy of 10.4×10^6 joules/kg (4500 Btu/lb), and Reynolds numbers, Re , based on body length of 0.04×10^6 and 0.023×10^6 . Thermal paint isotherms, oil flow patterns, and flow visualization data were obtained at $M_\infty = 14$, $Re = 0.035 \times 10^6$, and at $M_\infty = 10$ and $Re = 0.41 \times 10^6$. Shadowgraphs were obtained at $M_\infty = 5.2$ and 10.4 at $Re = 0.9 \times 10^6$ and 1.1×10^6 , respectively, and at $M_\infty = 5$ and $Re_{\infty, 2} = 1.5 \times 10^6$.

Heating of the configuration is generally concentrated at the nose, pitch control, and fin leading edges at low angles of attack and at the lower surface, pitch control, and extended rudders at high angles of attack. The data for the lower body surface are compared with theoretical estimates at angles of attack from 0° to 77° . Good agreement was obtained with the theory of Lees for axisymmetric shapes at 0° angle of attack and with local swept-cylinder theory at angles of attack above 21° . The dual lower pitch controls of the M2 configuration experienced heating rates considerably in excess of body stagnation rates at an angle of attack of 14° . Heating of the single pitch control of the M2-F2 configuration, however, was substantially reduced and was generally less than 50 percent of the body stagnation-point heating rate. Three-dimensional separated flow occurred in the region of the lower pitch controls and extended rudders in all tests at the lower angles of attack.

INTRODUCTION

This investigation is part of the current NASA research effort to develop lifting-entry vehicles with horizontal landing capability. Some of the results of this work at Ames Research Center are the configurations known as the M2 series. The most recent configuration of this series, the M2-F2, has been designed for stable, hypersonic flight at angles of attack that permit modulation of the lift-drag ratio from near 0 to about 1.3. The modulation of hypersonic lift-drag ratio, which permits the selection of landing sites unavailable to a ballistic vehicle, involves the use of aerodynamic controls to obtain stable flight at the required attitude. The extension of aerodynamic control surfaces into the complex flow surrounding these vehicles must be done judiciously, however, to minimize the heating penalties associated with all


*Title, Unclassified.

[REDACTED]

such controls. In view of the considerable effort which has been expended in the aerodynamic development of the M2 series (see refs. 1-23), it is appropriate to examine the convective heating of these configurations with the aerodynamic controls required for stable flight at hypersonic speeds.

SYMBOLS


A	planform reference area
C	calorimeter specific heat
C_F	vertical-tail chord
C_L	lift coefficient
c_1	M2 pitch-control chord
c_2	M2-F2 pitch-control chord
H	rudder span
H_t	total enthalpy
$\frac{L}{D}$	lift-to-drag ratio
l	M2 body length
M_∞	free-stream Mach number
p	surface pressure
p_0	model stagnation pressure
p_t	stream total pressure
p_{t_2}	total pressure in the body flow behind the bow wave
q	local heat-transfer rate
q_0	stagnation-point heat-transfer rate
\bar{q}	average control heat-transfer rate
\bar{q}_0	ratio of stagnation-point heat-transfer rate to the maximum stagnation heating of the entry trajectory
$Re_{\infty, l}$	body length Reynolds number based on free-stream properties
R_0	primary nose radius $\left(\frac{l}{12}\right)$


S' body-surface distance from the cone axis at the nose
S₁ M2 pitch-control span
S₂ M2-F2 pitch-control span
T_t flow total temperature
T_w wall temperature
t time
W weight
x model axial coordinate
y model lateral coordinate
z model vertical coordinate
α angle of attack with reference to cone axis
β angle of yaw
γ specific-heat ratio
γ_E trajectory entry angle
δ_p pitch-control deflection angle
δ_r rudder deflection angle
η normal distance from body surface
ρ free-stream density
ρ_c model calorimeter density
τ model skin thickness
φ body roll coordinate

EXPERIMENT

Test Facilities

Three test facilities were utilized for this investigation. The calorimeter heat-transfer data were obtained in the Ames 1-foot shock tunnel. Other measurements in this facility include thermal paint isotherms, surface flow visualization, and self-illumination photography. In the shock tunnel a large




combustion driver generates test flows at a velocity of 4,250 meters per second. In the present configuration the tunnel has a running time of about 25 milliseconds. A more detailed description of the shock tunnel is given in reference 24. Shadowgraphs, surface flow visualization, and thermal paint isotherms were also obtained in the Ames 3.5-Foot Hypersonic Wind Tunnel. This tunnel (described in ref. 25) is an intermittent, blowdown-type facility with a large pebble-bed heater. A quick-insert model-support mechanism capable of plunging the model into the flow in approximately 1/4 second was used for the tests in the 3.5-foot tunnel to eliminate the influence of the tunnel starting and stopping processes on the model paint isotherms and surface flow features. The third facility is the continuous flow 10- by 14-inch supersonic wind tunnel described in reference 26. Shadowgraphs from this tunnel taken during the work of reference 9 are used for comparative purposes in this investigation.

The various test conditions in the three facilities are tabulated below:

Type of Test	Facility	M_∞	$Re_\infty, \text{in} \times 10^6$	p_t, atm	$H_t, \text{J/kg} \times 10^6$	$T_t, ^\circ \text{R}$	Nozzle
Calorimeter, self-luminous photography	Shock tunnel	10.0	0.023, 0.04	310.0	10.4	---	4.5° half-angle conical
Paint, and oil flow	Shock tunnel	14.0	0.035	310.0	10.4	---	10° half-angle conical
Paint, and oil flow	3.5-foot tunnel	10.4	0.41	28.0	---	2100	Axisymmetric contoured
Shadowgraph	3.5-foot tunnel	5.2	0.85	7.7	---	2100	Axisymmetric contoured
Shadowgraph	3.5-foot tunnel	10.4	1.07	69.0	---	2100	Axisymmetric contoured
Shadowgraph	3.5-foot tunnel	10.4	0.55	69.0	---	2100	Axisymmetric contoured
Shadowgraph	10x14-inch tunnel	5.0	1.9	5.9	---	660	Two-dimensional contoured

Test Models and Instrumentation

The M2 configuration, which has been well described in the literature (e.g., ref. 11), is derived from a blunted 13° half-cone with dual rudder controls. The aft portion of the body is boattailed and contains movable pitch controls on the upper and lower surfaces. The boattailing which is required for hypersonic pitch trimming also improves the subsonic landing performance by lowering the base drag. The M2-F2 is an improved modification of the basic M2 configuration in which the boattail is extended and the dual lower pitch controls are replaced with a single lower control. These changes resulted from some of the investigations of references 1 through 19. Dimensions of the


M2 and M2-F2 are given in figure 1 and photographs of some of the several types of models used in this investigation are seen in figure 2.


Two different sized models (figs. 2(a) and (b)), 15.24 and 8.9 cm long, were used to obtain the thermocouple data in the shock tunnel. The shorter model was supported with extensions of the dual rudders to reduce sting interference effects on the model base and upper surface at the higher angles of attack. These models were made with an investment casting procedure developed at Ames which uses a silicon-bronze alloy combining good casting properties, strength, and known thermal properties. The wall thickness of the finished models was measured at each thermocouple location and was nominally 0.38 mm (0.015 inch). Thermal response times were computed for all models, and typical values were found to be about 6 milliseconds. The pitch controls for the models were formed from type 302 stainless steel sheet; those for the M2 were 0.27 mm thick and for the M2-F2, 0.152 mm thick. Since the forebody of the M2 and M2-F2 are identical, measurements were made only on the M2 body and the M2-F2 model body was an uninstrumented thick-wall casting of copper alloy.

Because of the slight variation in tunnel conditions from run to run caused by the combustion driver of the 1-foot shock tunnel, a hemisphere 2.54 cm in diameter was tested simultaneously with the M2-F2 and 8.9 cm M2 models, and the heating rates measured at the stagnation point of the hemisphere were used to make the model heating rates dimensionless. The hemisphere data were adjusted with the usual inverse square root relation to compensate for the smaller radius at the nose of the 8.9 cm M2 model. The hemispheres were also cast of the same silicon-bronze alloy used for the M2 models. All the calorimeter models were instrumented with No. 36- and 40-gage chromel-constantan thermocouple wire, 0.127 and 0.089 mm (0.005 and 0.0035 inch) in diameter, which was spot welded to the inside surface of the model skin.

The models used for the 3.5-foot tunnel tests were 33.8 cm long and were made by slush-casting an aluminum-oxide and silicon-dioxide slurry on the inside surface of a thermoplastic mold. The green ceramic casting, approximately 0.65 cm thick, was oven fired at 1060° C for 4 hours. A supporting sting socket was then potted in the cooled ceramic shell with an aluminum-filled epoxy. The temperature-time histories of the model surface during the tests indicate that the thermal diffusivity of the sintered ceramic material was lower than the published values for dense aluminum oxide. This was beneficial in preserving the details of localized heating on the surface of the model. The finished ceramic models were sprayed with a commercially available temperature-sensitive paint prior to testing.

Data Reduction

The thermocouple heating data were obtained in the shock tunnel by means of the thin-skin, transient-temperature technique in which the model of known thermal capacity is subjected to a step change in thermal environment. The rate of heat storage in the model skin may then be determined from the time rate of change of skin temperature according to the relation:



$$q_{\text{stored}} = \rho_c C \tau \frac{dT_w}{dt}$$

The heat stored in the model skin is a result of the complete thermal process described by the following heat balance relation:

$$q_{\text{stored}} = q_{\text{convection net}} + q_{\text{radiation net}} + q_{\text{conduction net}}$$

An examination of the various terms in this relation indicated that the conduction term could be minimized with suitable model-thermocouple design. Total radiant exchange and convective processes at the inner surface of the model skin are also negligible; therefore, q_{stored} is considered equal to $q_{\text{convective}}$ (aerodynamic) and no corrections have been made to the raw data.

Because of the complexity of the test configurations, an additional test technique was used to supplement the limited spatial resolution of the thermocouple measurements. Temperature indicating paints were applied to the 3.5-foot and shock-tunnel models to indicate areas of localized heating that might not be detected with the thermocouple measurements. The ceramic models tested in the 3.5-foot tunnel were sprayed with a four-color-change temperature-sensitive paint. Isothermal contours were readily observed on these models as lines separating two adjacent colors. For the conditions of the 3.5-foot tunnel tests these isothermal contours qualitatively represent lines of constant heating rate.

The color change paint was not used in the shock tunnel because of the short test duration. Instead, a flat black lacquer was applied to the model surface in sufficient thickness to prevent heat diffusion through the paint to the model surface during the 25 millisecond testing time. The paint surface temperature distribution is thus related to the local heating rate and the influence of the model construction (part thin skin, part heavy wall) is minimized. Since the flow in the shock tunnel is terminated with an explosively actuated nozzle valve and the flow starting process is very short compared with the test time, step change conditions are closely approximated. This step change in flow allows the resulting model surface isotherms, which are visualized in the paint and are the integrated result of the entire heating process, to be related to the heat-transfer distribution. The visualization of the isotherm is thought to result from the process described in reference 27 in which a thin film is formed on the surface of the paint by the aerodynamic heating process. The thickness of this film is related to the local heating rate since all surfaces of the model are exposed to the flow for the same time. Isothermal contours can be observed after the test as regions of constant color in the interference patterns in light reflected from the surface. The heating ratios obtained by this technique were derived from comparisons with the calorimeter data.

Entry Trajectories

Before beginning the discussion of the test results it is instructive to examine some representative near-earth-orbit entry trajectories for the M2-F2 and to compare the flight environment with the test conditions of this investigation. Three representative, lift-modulated entry trajectories that require flight at angles of attack from near 0° to almost 40° are presented in Figure 3. Free-stream Reynolds numbers based on the 6.75 meter length of the M2-F2 vehicle are shown for several points in the entry. The flight Reynolds numbers are found to be rather low, generally increasing from about 1×10^5 during the peak heating of the pullout maneuver to about 1×10^6 at a velocity of 3 km/sec. The stagnation-point heating rate, which has been made dimensionless with respect to the peak heating at pullout, is also shown for several positions in the $L/D = 1.0$ trajectory. Notice that for these entry trajectories the Reynolds numbers stay below approximately one million until the stagnation-point heating rate has dropped to almost one quarter of the peak value. The flight Reynolds numbers of approximately 1 to 2×10^5 during the high-heating portion of the entry may be compared with Reynolds numbers of 0.2 and 0.4×10^5 for the shock-tunnel tests and 4×10^5 and 1×10^6 for the 3.5-foot tunnel tests. No evidence of boundary-layer transition was seen in the present tests and the data are believed to be representative of laminar flow.

In the comparison of the experimental test conditions of this investigation with the environment expected in flight, the questions of Mach number duplication, wall-temperature ratio, and chemical similitude also must be considered. With reference to the work of references 28 and 29 it is believed that the Mach number range of the present tests (10 and 14) is sufficiently high to demonstrate the essential features of the total pressure distribution in the flow about this blunted, slender body. The ratio of wall temperature to flow stagnation temperature was found to be approximately 0.06 for the shock-tunnel conditions and to vary from about 0.5 to 0.7 for the 3.5-foot and 10- by 14-inch tunnels. In flight, ratios of approximately 0.2 to 0.4 are expected for the various trajectories and vehicle surface temperatures that may occur.

The last item to be considered here is the degree to which the various flow fields of the present tests simulate the chemical aspects of the flow to be expected in flight. The low-temperature flows of the 10- by 14-inch and 3.5-foot tunnels are, of course, in chemical equilibrium and will not be considered in this discussion. A criterion proposed in reference 30 was found to be helpful in this regard and was used in estimating the degree of chemical similitude of the shock-tunnel and flight conditions. Briefly, this criterion involves a comparison of the detachment distance of the body bow shock in the model flow to the reaction distance required for the maximum in the concentration of the NO species to be obtained in a corresponding nonequilibrium planar flow of air behind a normal shock. If these two distances are of the same order, then the three-body recombination reactions in the inviscid model flow are relatively unimportant, and two-body or binary scaling (ρR_0) concepts may be used to relate the flow to other two-body dominated flows at the same

[REDACTED]

velocity. To determine the degree to which this concept can be applied to the present tests, nonequilibrium real-gas calculations were made for the shock-tunnel conditions by the method of reference 30. The reaction distance required for the maximum NO concentration to be reached was found in the calculations to be two orders of magnitude greater than the model bow-shock detachment distance. This indicates that a two-body dominated flow with relatively unimportant recombination processes was obtained in the shock-tunnel tests. Since, in the calculation, the nose flow was found to be out of equilibrium in the dissociation process, some frozen energy of dissociation may be present in the expanding afterbody flow. Because of the nonequilibrium expansion of the flow in the shock-tunnel nozzle, however, the dissociation level in the flow between the bow shock and the body nose is greater than it would be in an equilibrium free stream, and the resulting flow about the shock-tunnel model is believed to approach the flight condition more closely than indicated by the ρR_0 product.

The flight and shock-tunnel conditions were compared on the basis of ρR_0 scaling, and the computed condition is shown in figure 3 as the single-filled symbol. The product ρR_0 for the shock-tunnel test is less than the desired flight value (on the basis of free-stream density, ρR_0 matching occurs at an altitude above the desired trajectory). Consequently, the flight flow would more closely approach equilibrium at the nose than would the shock-tunnel flow. The previously mentioned NO criterion did, however, indicate that a two-body dominated flow may also be expected for the flight condition at the shock-tunnel flow velocity. It is believed from the results of this analysis, therefore, that the shock-tunnel results approximate to a reasonable degree the chemical aspects of the inviscid body flow at the test velocity.

Body Test Results

Body pressure distribution.- Several theoretical lower surface pressure distributions for an angle of attack of 0° are shown in figure 4. These theoretical distributions are compared with data from 3.5-foot tunnel tests of reference 11 since no data for the shock-tunnel conditions are available. The theoretical curves were obtained from the modified Newtonian theory used in reference 31 and from computer calculations using the method of characteristics and assuming shock-tunnel conditions for equilibrium and frozen ($\gamma = 1.4$) flow. It should be mentioned that the M2 nose shape is contoured in the region of the juncture with the cone and therefore differs slightly from the cone-hemisphere shape used for the two theoretical axisymmetric pressure distributions. A point of interest was observed in the characteristics solutions of reference 28 which show an undershoot in the cone surface pressure several nose radii aft of the blunt nose which slowly recovers to the Newtonian value at $x/R_0 \approx 20$. In this sense the M2 is a short body and the cone flow may be expected to be substantially influenced by the blunt nose at low angles of attack. Also, as shown in reference 28, the undershoot in cone pressure on this short body is not expected to change appreciably with increasing Mach numbers above 10.

Body heating distributions.- The longitudinal body heating distributions are shown in figure 5. The heating data of this investigation are plotted in

the dimensionless ratio form of local heat-transfer rate, q (in energy per unit area per unit time), to the stagnation-point heating rate of a sphere, q_0 , having the same radius as the major radius at the nose of the M2. The body surface position is measured from the intersection of the axis of the cone with the nose and is made dimensionless with the major nose radius which is equal to 0.08337. In the figures for the longitudinal centerline distributions (5(a)-5(e)), the upper surface data are shown on the right and the lower surface data on the left.

A general feature of the data is that the higher heating rates are concentrated at the nose at the low angles of attack. Indeed, heating of the body aft of the nose at $\alpha = 0^\circ$ is below 10 percent of the stagnation rate. In figure 5 at $\alpha = 0^\circ$ three theoretical curves are shown for the lower surface heating distribution. The theory of reference 31 (Lees') is used with the Newtonian pressures of figure 4, and with the measured pressure distribution of reference 11 which was obtained in the 3.5-foot tunnel at a Mach number of 10.4 and a Reynolds number of 0.5×10^6 . The third theoretical curve was obtained by adjusting the experimental pressure distribution of reference 11 to include the effects of the source flow in the conical nozzle of the shock tunnel. The theory of reference 32 was used for this calculation and nozzle boundary-layer effects were neglected. It may be seen that excellent agreement with the present data is obtained with this calculation. One additional factor to be considered, however, is the effect of the viscous induced pressures on the body at low angles of attack. The results of reference 33 indicate that because of increased boundary-layer thickness the conical-body pressures in the shock-tunnel flow may be expected to be approximately 5 to 10 percent higher relative to nose stagnation pressure than those measured in the 3.5-foot tunnel. This increased pressure would, of course, result in a slight increase in the local cone heating relative to the theoretical value. It is believed, nevertheless, that the present tests indicate relatively little influence of the nonequilibrium inviscid flow on the body heating distributions.

On the upper surface at $\alpha = 0^\circ$, the influence of a large spherically blunted canopy is seen in the low value of body heating just upstream of the windshield. Apparently a region of separated flow is created by the canopy. A region of separation was also observed in shadowgraphs of this body for other test conditions which will be shown in a later figure. The three data points obtained on the top of the body at the side of the canopy serve to illustrate the heating that might be expected in the absence of a canopy. The data for an angle of attack of 14° are shown in figure 5(b). This attitude is representative of flight at the maximum lift-to-drag ratio for this vehicle. The influence of the canopy on the top surface may still be seen although the level of the top-surface heating is reduced by a factor of approximately 2 from the $\alpha = 0^\circ$ values. The lower conical surface heating ratio, however, has increased from 0.06 to about 0.2. The theoretical calculation for figure 5(b) was made with Newtonian pressures because of the approximate nature of the tangent-cone assumption required in the application of the theory.

The data for 21° angle of attack are shown in figure 5(c). These and succeeding data at higher pitch angles were obtained with the smaller 8.9 cm model, which was supported with twin rudder extensions, so that heating could

be measured on the base and upper surface of the model at the higher angles of attack. At this attitude ($\alpha = 21^\circ$) the influence of the aft canopy on the upper surface heating has essentially vanished. The lower surface heating has increased to about 0.3. The theory of reference 31 as used here substantially underestimates the level of the data due to the developing crossflow on the pitched cone. A simple local swept-cylinder prediction is found, however, to give good agreement at this higher pitch attitude. The factor $\sqrt{2}$ of reference 34 was used to relate the three-dimensional spherical heating of the nose to a cylindrical stagnation line value, and a simple cosine variation was used in this and the remaining figures to account for the sweep angle of the lower meridian. The axial variation was obtained with the one-half power of the ratio of the local body radius to the nose radius. The base-heating data in figure 5(c) taken at the center of the flat base area are at about the level of the heating on the top surface at the rear of the body (about 0.25 percent of the reference value). Note also in figure 5(c) that the heating on the aft lower surface at the side of the boattail ($S'/R_0 = 9.8$, $\phi = 135^\circ$) is almost twice that at the same longitudinal station on the lower meridian. This is attributed to the two-dimensional boattailing of this three-dimensional body which apparently results in an appreciable thinning of the boundary layer at the side or corner of the boattail. This variation may be more readily seen in the circumferential distributions that follow.

The data in figures 5(d) and 5(e) represent distributions for flight near maximum lift coefficient and the special case where the lower cone element is normal to the flow. At this attitude, $\alpha = 77^\circ$, the nose heating does not reach the reference value. Model markings after the test show that the boundary-layer flow away from the body meridian was not normal to the forward cone element but was inclined slightly toward the nose, indicating that a stagnation-line type of flow would be obtained at an angle of attack slightly less than 77° . This effect is caused by the increasing radii of the conical cross sections. A similar effect was found in reference 35 where the maximum stagnation line pressures for a 15° cone occurred at a meridian pitch angle of about 80° . Corresponding results may be seen in figure 6 in which the lower-surface heating at the midpoint of the cone is shown as a function of the lower-meridian pitch angle. The maximum heating occurs at a deflection angle somewhat less than 90° . Also included in the figure are the calculations for cone element pitch angles of 13° and 27° shown in figure 5 which use both measured and Newtonian pressures. With these two theoretical approaches, good agreement is obtained with the data for the entire angle-of-attack range.

Circumferential heating distributions. - The circumferential heating distributions of the body including the aft canopy are shown in figures 7(a) to 7(e). The data are plotted with the position angle ϕ measured from the upper meridian. The influence of the canopy and the development of the windward-leeward flow may be seen in the figures. The increased heating at the side of the lower boattail surface at station $x/l = 0.760$ which was mentioned previously can also be seen in figures 7(b), (c), and (d).

Flow visualization.- Because of the complexity of the flow in the vicinity of the controls, shadowgraphs and other visual data will assist in the analysis of the heating results. Shadowgraphs of the flow about the M2 are presented in figures 8(a), (b), and (c). Figures 8(a) and 8(b) were obtained from the work of reference 9 which was performed in the Ames 10- by 14-Inch Supersonic Wind Tunnel at a Mach number of 5.0. Both lower control shocks are seen in figure 8(b) because the model was rolled slightly and the shadowgraph light source was not precisely in line with the two controls. Figure 8(c) was taken during tests in the 3.5-foot tunnel at a Mach number of 10.0 with the same model configuration and attitude shown in figure 8(a). The test conditions for these shadowgraphs are listed on the various figures. Although these photographs represent nearly adiabatic wall conditions and therefore tend to overemphasize the degree of separation that would be present with a cold wall at the same conditions, the general feature to be observed is that the body boundary layer is separated by the deflected pitch controls and that the extent of the three-dimensional separation is influenced by the body pitch attitude.

The condition of the model after the shock-tunnel tests is shown in figure 9. These tests were performed at a Mach number of 10 with the same pitch control deflection and attitude shown in figure 8(b). The discolored areas on the face of the pitch controls are believed to represent the reattachment zone of the separated body boundary layer. Other markings are also visible on the body surface in figure 9(b) and are apparently associated with the flow in the separated area. The three-dimensional character of the entire separation region is indicated by the curvature visible in the reattachment zone markings.

Inviscid total pressure distribution.- A factor which should be considered in a discussion of flow over the controls of blunt-nosed slender bodies is illustrated in figure 10. In this figure the normalized total pressures are shown for the inviscid flow between the shock envelope and the body surface of a blunted 15° cone. The solutions were obtained with the method of characteristics and are for the ideal gas flow of air at several Mach numbers. These distributions, which are dependent upon longitudinal station, were computed for a body station (x/R_0) of 5.00. For relatively short bodies such as the M2, however, the distributions shown are representative. Note the substantial variation in total pressure in this blunt-nose dominated flow field. Notice also that at higher Mach numbers the region of low total pressure near the body occupies an increasingly large portion of the inviscid shock layer. It is to be expected therefore that the flap-type controls that extend into this nonuniform flow may experience substantial variations in surface pressures and heating.

M2 pitch-control heating.- The pitch-control heating distributions for the M2 are shown in figures 11 and 12. These data were obtained in the shock tunnel for $\alpha = 0^\circ$ and 14° with the approximate control deflections required for trim. In general, the results show increased heating from the hinge line aft in the longitudinal distributions and increased heating at the outer edge of the controls in the spanwise distributions. This result is indicative of the three-dimensional separation and reattachment of the body boundary layer

~~SECRET~~

in the presence of the previously discussed nonuniform flow which surrounds the body. The maximum level of heating for these M2 controls was 40 percent of the reference value at $\alpha = 0^\circ$ and 340 percent at $\alpha = 14^\circ$. (Local control heating considerably in excess of the body stagnation value was also observed in a previous work (ref. 36). With the assumption that the prominent dark band seen on the face of the pitch controls in figure 9 represents the zone of reattachment of the body flow on the controls, a limited comparison of the extent of separation may be made with the shadowgraph of figure 8(b) from the tests at $M = 5$. Although the three dimensionality of the flow in the separated region makes a quantitative comparison difficult, measurements indicate that the extent of separation in the $M = 10$ shock-tunnel flow may be similar to that in the 10- by 14-inch tunnel tests at $M = 5$ at the model pitch attitude of 14° .

M2-F2 Single Pitch Control

Pitch trim and flow visualization.- The pitch control deflection angles required for longitudinal trim of the M2-F2 at hypersonic speeds and angles of attack up to 37° are presented in figure 13 to assist in the interpretation of the heating data that follow.

These pitch-trim results were taken from the recent work of Axelson (ref. 37) which was performed in the 3.5-foot tunnel. Shadowgraphs of the flow over the M2-F2 pitch control during tests in the 3.5-foot tunnel are seen in figure 14. These shadowgraphs compare flow over the control at Mach numbers 5 and 10 in the 3.5-foot tunnel for attitudes near maximum lift-drag ratio and maximum lift. Natural illumination pictures of the flow over the pitch control in the shock tunnel, and a thermal paint photograph are presented in figure 15.

A comparison of figures 14(a) and (b) which were taken at Mach numbers of 5 and 10 at the attitude for maximum lift-drag ratio shows an increase in the extent of control separation at Mach 10. The corresponding figures 14(c) and (d), however, show no effect of the increased Mach number on the limited extent of control separation which occurs at the higher pitch attitude of 30° . The flow visualization information for the M2 and M2-F2 is summarized in table I with the comparable model configurations indicated with brackets. Two points may be noted from an inspection of these tabulated results: The extent of control separation on the M2 at $\alpha = 0^\circ$, and on the M2-F2 at $\alpha = 15^\circ$, is apparently increased with increasing Mach number whereas the combined effects of low wall-temperature ratio and low Reynolds number tend to decrease the extent of separation on the M2-F2 at $\alpha = 15^\circ$ in the shock-tunnel flow. In contrast, the much less extensive separation on the M2 at $\alpha = 14^\circ$ and on the M2-F2 at $\alpha = 30^\circ$ is apparently insensitive to the various test conditions. From a comparison of the M2 and the M2-F2 it is believed that the aft mounted control of the M2-F2 is more extensively shielded by the boattail and therefore retains sensitivity to the previously mentioned total-pressure gradients and to body boundary-layer development to a higher pitch attitude than do the more forward positioned controls of the M2. The increased aspect ratio of the wider M2-F2 control would also be expected to influence the extent of separation and this may be seen in the table for comparisons of similar pitch

TABLE I.- FLOW VISUALIZATION SUMMARY OF BOUNDARY-LAYER SEPARATION
IN THE REGION OF THE LOWER PITCH CONTROLS

α , deg	δ_p , deg	M_∞	Re_∞, l	T_w/T_t	Percent separation	Source	Figure
M2							
[0	45	5.0	1.9×10^6	0.7	40	Shadowgraph ^a	8(a)
	45	10.4	$.5 \times 10^6$.63	70	Shadowgraph ^b	8(c)
[14	45	5	1.9×10^6	.7	20	Shadowgraph ^a	8(b)
	45	10	$.04 \times 10^6$.06	20	First edge of burn mark ^c	9
M2-F2							
[15	35	5.2	$.85 \times 10^6$.5	40	Shadowgraph ^b	14(a)
	35	10.4	1.07×10^6	.5	70	Shadowgraph ^b	14(b)
[30	15	5.2	$.85 \times 10^6$.5	Nil	Shadowgraph ^b	14(c)
	15	10.4	1.07×10^6	.5	Nil	Shadowgraph ^b	14(d)
[15	40	10	$.04 \times 10^6$.06	40	Natural illumination ^c	15(b)
	40	14	$.035 \times 10^6$.06	25 edge 50 center	Paint markings ^c	15(d)

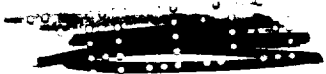
^a10- by 14-inch tunnel

^b3.5-foot tunnel

^c1-foot shock tunnel

attitudes and control deflections. One important aspect of this configuration with respect to control separation is the stabilizing influence of the favorable pressure gradient (caused by the boattail) on the body boundary layer.

Exploratory oil flow tests were performed in both the 3.5-foot tunnel and the shock tunnel and photographs of the results are presented in figure 16. In comparing the oil flow results which at first appear quite different, it is necessary to consider that the visualization materials used are sensitive to the product of the local heating rate and the test time. The shock-tunnel test was of such short duration that the graphite-grease did not melt and flow on all parts of the model, whereas in the 3.5-foot tunnel test the colored paraffin was melted from both the nose and the control. A limited qualitative indication of the surface shear, flow direction, and relative heating may be obtained, however, from the figures. Some details of the control edge flow may be seen on the shock-tunnel model and the separation line upstream of the control is visible on the 3.5-foot tunnel model. Notice also in both tests the substantial component of surface cross flow near the nose at this low angle of attack.



M2-F2 pitch control heating.- The pitch-control heating distributions obtained for the M2-F2 in the shock tunnel are presented in figures 17 to 23. Both longitudinal and spanwise distributions are shown for angles of attack of 0° , 15° , and 20° . One test was made at combined pitch and yaw angles of 15° and the results are shown in figure 21. A general feature of the data, as in the M2 results, is the increase in heating at the rear and outer edges of the control. In three instances, however, at $\alpha = 15^\circ$ (figs. 18, 20, and 21) maximum heating occurred forward of the control trailing edge. This is believed to indicate that the local boundary-layer reattachment process has been completed in these areas. Data were also obtained on the flat side of the control near the edge for two conditions and may be seen in the spanwise distributions of figures 18 and 21. In figure 18 which is for the unyawed body the side heating is seen to be relatively low and is similar in level to the heating of the face of the control near the hinge line. For the yawed attitude, however, when the instrumented side is upwind (fig. 21(b)), heating of this surface substantially exceeds that of the forward face of the control and reaches a level of about 0.7. It is indicated, therefore, that consideration must be given to the protection or elimination of actuating mechanisms near the sides of flap-type controls.

To summarize the previous figures, longitudinal heating distributions are presented in figures 22 and 23 showing the edge and center heating for the unyawed tests. Reference may be made to figure 13 for the control deflections required for trim. Note the substantial increase in heating at $\alpha = 15^\circ$ when the control deflection is increased from 30° to 40° . The required deflection for trim at this attitude is 33° for the moment center given in figure 1. It is apparent that changes in vehicle configuration that require additional control deflection for trim may substantially increase the heating load to the control.

A comparison of the M2 and M2-F2 control heating is given in figure 24. The dashed line represents heating data for the boattail area of the body ($\delta_p = 0^\circ$). It is evident that the heating rate of the M2-F2 control is substantially less than that of the M2. Total heat load comparisons must, of course, include the factor of 2 increase in exposed surface area of the larger control. A comparison of the relative effectiveness of the two controls based on the geometrical considerations of the larger M2-F2 control and the increased leverage obtained from the more aft position shows that the required pressure on the M2-F2 control is approximately $1/3$ of the value required for the dual M2 controls. The relative heating of the two control systems which might be expected at the location of boundary-layer reattachment was estimated from the data of reference 38. These estimates, which ignore the three-dimensional character of the control flow, indicate that a reduction in heating by approximately a factor of 4 might be expected for the M2-F2 control. It may be seen in the figure, however, that substantially larger differences were measured. This is believed to be a result of the highly three-dimensional flow over the narrower M2 controls. In summary, it is seen that with careful design it appears possible to avoid excessive control heating while still maintaining sufficient control effectiveness for trimmed flight.

M2 fin and rudder heating.- Two photographs and a sketch of the results of an oil flow test in the shock tunnel at $\alpha = 0^\circ$ are shown in figure 25. Localized heating at the top of the deflected rudders may be seen in both photographs. In later figures, this area of localized heating will be seen to move to the lower edge of the rudder as the angle of attack is increased. The surface flow on the deflected rudders has been visualized with streaks left by the melted or vaporized graphite grease. It may be seen that the surface flow is highly three-dimensional on the upper surface of the deflected outboard rudders. Apparently the combined effects of the impingement of the fin leading-edge shock on the upper rudder edge and the increased body boundary-layer thickness at the lower edge of the rudder are sufficient to cause this downward flow at $\alpha = 0^\circ$. In figure 16(c) evidence of an upward flow parallel to the rudder hinge line may be seen after a test at an angle of attack of 15° . The existence of this parallel flow which changes direction with pitch angle should be considered in the design of hinge mechanisms and aerodynamic seals.

The results of measurements made in the shock tunnel of the fin and rudder heating are seen in figure 26. Two angles of attack were tested, 0° and 14° . The fin leading-edge heating is relatively low at $\alpha = 0^\circ$, increasing from 0.15 near the body to about 0.25 near the upper edge. An indication of the nonuniformity of shock-layer flow about this blunt slender shape may be seen in these heat-transfer measurements in which the swept leading edge of the fin intercepts a cross section of the body flow field. The fin-rudder heating at $\alpha = 14^\circ$ is seen in figure 26 to be approximately one order of magnitude lower than that at $\alpha = 0^\circ$, and at sufficiently high angles of attack a swept trailing-edge type of flow may be expected to develop at the fin leading edge. With reference to the previous discussion of hinge-line flow, note that the heating of the lower portion of the outer rudder (shown with an open triangular symbol) is increased by a factor of 2 as the pitch angle is increased to $\alpha = 14^\circ$.

Canopy heating.- The heating data for two proposed canopy configurations are shown in figure 27 for two angles of attack and one angle of yaw. The heating of both canopies is quite low for these attitudes with heating ratios between about 0.01 and 0.1 being measured. The more slender conical canopy has about the same level of heating at the forward location as the blunt canopy has in the aft position.

M2-F2 Temperature Visualization Results

Shock-tunnel results.- The thermal contours which were obtained with paint in the shock tunnel are shown in figure 28 (figures 2(c), 2(d) and 15(d) are photographs of the model after the test) for tests at $M_\infty = 14$ and $Re_{\infty, \tau} = 0.035 \times 10^6$. The numerical values of heating ratio are to be regarded as approximate only and were obtained from comparisons with local values obtained from the calorimeter measurements. These thermal-paint techniques are intended to supplement the limited spatial resolution of the thermocouple measurements which might miss entirely a small area of localized heating. In this sense the thermal paint results generally agree with the thermocouple

[REDACTED]

measurements, with one exception. The thermal paint patterns on the pitch control at $\alpha = 15^\circ$ and $\delta_p = 30^\circ$ (fig. 28(b)) did not indicate the increase in heating at the edge of the control which was found with the thermocouple measurements.

3.5-foot-tunnel results.- The data presented in figures 29 through 31 were obtained from tests in the 3.5-foot tunnel at a Mach number of 10 and Reynolds number of 0.5×10^6 . Figures 29 and 30 illustrate the changing model appearance during the course of the run as the isotherms advance over the surface of the model. The photograph in figure 29(c) taken after completion of the run reveals several details of the influence of the deflected control on the body surface. Evidence of intense local heating of the lower corner of the deflected rudder is also seen in the photograph. Figure 29(d) is a top view of the model after a test at $\alpha = 15^\circ$ showing the heating of the swept conical windshield. Figure 30 is a sequence of photographs showing the heating of the configuration at 30° angle of attack. In figure 30(b) a separation zone is indicated by the light colored area on the body just forward of the control. A separation shock is also faintly visible at approximately the same location in the shadowgraphs of figures 14(c) and (d). The separation and reattachment angles are apparently quite small and there is little evidence of the separated flow on the control. Indeed, the pitch-control heating as indicated by the appearance of the model in figure 30(c) is relatively mild at this attitude.

The photograph in figure 31 was taken after a test in the 3.5-foot tunnel at $\alpha = -7^\circ$. At this attitude, which corresponds approximately to the attitude for zero lift, the leading edges of the fins and the upper corner of the deflected rudders are exposed to a heating level similar to that of the body stagnation point. An interesting heating pattern is developed on the upper body surface from the interference of the flow developed behind the canopy shock at the intersection of the canopy and the body upper surface. In summary, the thermal paint technique was found to be quite useful and increased considerably the confidence level of the data with respect to spatial resolution.

CONCLUDING REMARKS

An experimental investigation has been conducted to determine the aerodynamic heat transfer to the Ames M2 and M2-F2 lifting entry bodies. The test conditions include Mach numbers of 5, 10, and 14 and several Reynolds numbers which span the range of those to be expected in flight. Calorimeter, oil flow, and thermal paint data were obtained in the 1-foot shock tunnel at a total enthalpy of 10.4 joules/kg (4500 Btu/lb). Oil flow, shadowgraphs, and thermal paint patterns were also obtained in the 3.5-foot hypersonic wind tunnel. Pressure distribution data from concurrent tests in the 3.5-foot and shadowgraphs from the 10- by 14-inch tunnel were also employed to assist in the analysis of the heating data. Analysis of the results has shown the following:

1. The heating of the configuration at low angles of attack is, in general, most intense on small areas at the nose, fin leading edges, and lower pitch control. At higher angles of attack the heat load is primarily imposed upon the body lower surface and extended controls.

2. The heating of the lower surface of the body at $\alpha = 0^\circ$ in the shock tunnel flow was well predicted by the theory of Lees' from the measured pressure distribution data from the 3.5-foot tunnel. Lower surface meridian heating at large pitch angles was predicted by a local swept-cylinder theory.

3. Deflection of the rudders and lower-surface pitch controls into the nonuniform three-dimensional flow surrounding this blunted body induced separation of the surface flow which was observed in all test facilities. The extent of separation was influenced by the control aspect ratio and position on the body as well as the control deflection and body pitch angle.

4. The extent of control induced separation was found in this investigation to increase with increasing Mach number and was reduced by the combined effects of strong wall cooling and decreased Reynolds number.

5. The heating of the larger pitch control of the M2-F2 was substantially less than that of the two smaller controls of the M2. Maximum local heating of the M2-F2 control at the body attitude for maximum lift-to-drag ratio was less than 1/3 of the nose stagnation value. It is apparent, therefore, that the pitch controls of this class of lifting body can be designed to provide the necessary trimming moments without incurring a severe heating penalty.

6. Heating of a highly swept, forward canopy and a larger aft-mounted canopy did not exceed 10 percent of the nose stagnation value at 0° angle of attack.

Ames Research Center

National Aeronautics and Space Administration
Moffett Field, Calif. 94035, June 7, 1968
124-07-01-03-00-21

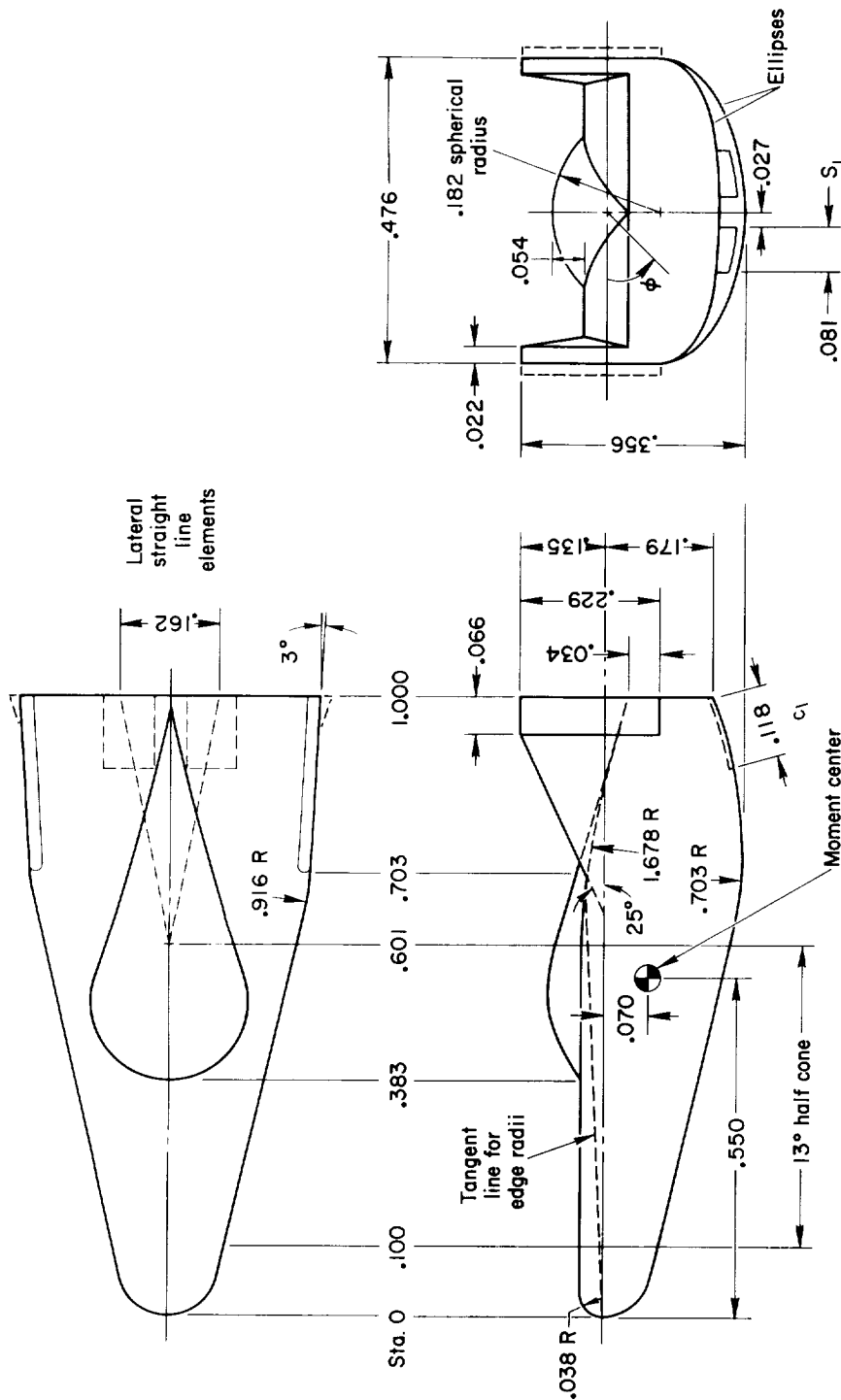
[REDACTED]

REFERENCES

1. Eggers, Alfred J., Jr.; and Wong, Thomas J.: Re-entry and Recovery of Near-Earth Satellites, With Particular Attention to a Manned Vehicle. NASA MEMO 10-2-58A, 1958.
2. Savage, Howard F.; and Tinling, Bruce E.: Subsonic Aerodynamic Characteristics of Several Blunt, Lifting, Atmospheric-Entry Shapes. NASA MEMO 12-24-58A, 1958.
3. Rakich, John V.: Supersonic Aerodynamic Performance and Static-Stability Characteristics of Two Blunt-Nosed, Modified 13° Half-Cone Configurations. NASA TM X-375, 1960.
4. Kenyon, George C.; and Edwards, George G.: A Preliminary Investigation of Modified Blunt 13° Half-Cone Re-entry Configurations at Subsonic Speeds. NASA TM X-501, 1961.
5. Weil, Joseph; and Matranga, Gene J.: Review of Techniques Applicable to the Recovery of Lifting Hypervelocity Vehicles. NASA TM X-334, 1960.
6. Dennis, David H.; and Edwards, George G.: The Aerodynamic Characteristics of Some Lifting Bodies. NASA TM X-376, 1960.
7. Kenyon, George C.; and Sutton, Fred B.: The Longitudinal Aerodynamic Characteristics of a Re-entry Configuration Based on a Blunt 13° Half-Cone at Mach Numbers to 0.92. NASA TM X-571, 1961.
8. Kenyon, George C.: The Lateral and Directional Aerodynamic Characteristics of a Re-entry Configuration Based on a Blunt 13° Half-Cone at Mach Numbers to 0.90. NASA TM X-583, 1961.
9. Rakich, John V.: Aerodynamic Performance and Static Stability Characteristics of a Blunt-Nosed, Boattailed, 13° Half-Cone at Mach Numbers From 0.60 to 5.0. NASA TM X-570, 1961.
10. Hassell, James L., Jr.; and Ware, George M.: Investigation of the Low-Subsonic Stability and Control Characteristics of a 0.34-Scale Free-Flying Model of a Modified Half-Cone Reentry Vehicle. NASA TM X-665, 1962.
11. Axelsson, John A.: Pressure Distributions for the M-2 Lifting Entry Vehicle at Mach Numbers of 0.23, 5.2, 7.4, and 10.4. NASA TM X-997, 1964.
12. Axelsson, John A.: Hypersonic Aerodynamic Characteristics of the Ames M2 Lifting Entry Configuration. NASA TM X-1301, 1966.
13. Syvertson, C. A.; Swenson, B. L.; Anderson, J. L.; and Kenyon, G. C.: Some Considerations of the Performance of a Maneuverable, Lifting-Body, Entry Vehicle. Advances in the Astronautical Sciences, Vol. 16, Part 1, American Astronautical Society, 1963, pp. 898-918.

- [REDACTED]
14. Spencer, Bernard, Jr.; and Phillips, W. Pelham: Low-Speed Aerodynamic Characteristics of a Modified Blunt 13° Half-Cone Lifting-Body Configuration Having Deployable Horizontal Tails With or Without Variable-Sweep Wings. NASA TM X-847, 1963.
 15. Horton, Victor W.; Layton, Garrison P., Jr.; and Thompson, Milton O.: Exploring New Manned Spacecraft Concepts. Astronautics and Aeronautics, vol. 2, May 1964, pp. 42-47.
 16. Mort, Kenneth W.; and Gamse, Berl: Full-Scale Wind-Tunnel Investigation of the Longitudinal Aerodynamic Characteristics of the M2-F1 Lifting Body Flight Vehicle. NASA TN D-3330, 1966.
 17. Horton, Victor W.; Eldredge, Richard C.; and Klein, Richard E.: Flight-Determined Low-Speed Lift and Drag Characteristics of the Lightweight M2-F1 Lifting Body. NASA TN D-3021, 1965.
 18. Smith, Harriet J.: Evaluation of the Lateral-Directional Stability and Control Characteristics of the Lightweight M2-F1 Lifting Body at Low Speeds. NASA TN D-3022, 1965.
 19. Love, Eugene S.: Manned Lifting Entry. Astronautics and Aeronautics, vol. 4, May 1966, pp. 54-64.
 20. Mort, Kenneth W.; and Gamse, Berl: Low-Speed Wind Tunnel Tests of a Full-Scale M2-F2 Lifting Body Model. NASA TM X-1347, 1967.
 21. McKinney, Linwood; Boyden, Richmond P.; and Taylor, Robert T.: Static Wind-Tunnel Investigation and Motion Studies of the M2-F2 Vehicle Launched From a Preliminary Location on the B-52. NASA TM X-1225, 1966.
 22. Anon.: A Theoretical Study of the Aerodynamic Characteristics of Lifting-Body Entry Vehicles. NASA CR-73025, 1966.
 23. Cahn, Maurice S.; Garcia, J. R.; and Andrew, G. M.: Rotational Apparent Mass by Electrical Analogy. NASA CR-73080, 1966.
 24. Cunningham, Bernard E.; and Kraus, Samuel: A 1-Foot Hypervelocity Shock Tunnel in Which High-Enthalpy, Real-Gas Air Flows Can Be Generated With Flow Times of About 180 Milliseconds. NASA TN D-1428, 1962.
 25. Holdaway, George H.; Polek, Thomas E.; and Kemp, Joseph H., Jr.: Aerodynamic Characteristics of a Blunt Half-Cone Entry Configuration at Mach Numbers of 5.2, 7.4, and 10.4. NASA TM X-782, 1963.
 26. Eggers, Alfred J., Jr.; and Nothwang, George J.: The Ames 10- by 14-Inch Supersonic Wind Tunnel. NACA TN 3095, 1954.
 27. Bloxsom, D. E.; and Rhodes, B. V.: Journal of the Aerospace Sciences, vol. 29, no. 12, Dec. 1962.

- [REDACTED]
28. Cleary, Joseph W.: An Experimental and Theoretical Investigation of the Pressure Distribution and Flow Fields of Blunted Cones at Hypersonic Mach Numbers. NASA TN D-2969, 1965.
 29. Seiff, Alvin; and Whiting, Ellis: The Effect of the Bow Shock Wave on the Stability of Blunt-Nosed Slender Bodies. NASA TM X-377, 1960.
 30. Hall, J. Gordon; Eschenroeder, Alan Q.; and Marrone, Paul V.: Blunt-Nose Inviscid Airflows With Coupled Nonequilibrium Processes. J. Aerospace Sci., vol. 29, no. 9, Sept. 1962.
 31. Lees, Lester: Laminar Heat Transfer Over Blunt-Nosed Bodies at Hypersonic Flight Speeds. Jet Propulsion, vol. 26, no. 4, April 1956, pp. 259-269, 274.
 32. Inouye, Mamoru: Numerical Solutions for Blunt Axisymmetric Bodies in a Supersonic Spherical Source Flow. NASA TN D-3383, 1966.
 33. Lewis, Clark H.; and Whitfield, Jack D.: Theoretical and Experimental Studies of Hypersonic Viscous Effects. AGARDograph 97, Part III, May 1965.
 34. Hayes, Wallace D.; and Probstein, Ronald F.: Hypersonic Flow Theory. Academic Press, 1959.
 35. Conti, Raul J.: Laminar Heat-Transfer and Pressure Measurements at a Mach Number of 6 on Sharp and Blunt 15° Half-Angle Cones at Angles of Attack Up to 90° . NASA TN D-962, 1961.
 36. Seegmiller, H. Lee; and Reller, John O., Jr.: An Experimental Investigation of the Convecting Heat Transfer to a Blunt Lifting Body With Controls. NASA TM X-785, 1963.
 37. Axelsson, John A.; and Mellenthin, Jack A.: Hypersonic Aerodynamic Characteristics of the M2-F2 Lifting Entry Configuration. NASA TM X-1690, 1968.
 38. Holden, Michael: Separated Flow Studies at Hypersonic Speeds. Part II - Two Dimensional Wedge Separated Flow Studies. Cornell Aero. Lab. Rep. AF-1285-A-13(2), Dec. 1964.



Note : All dimensions based on model length l

Present tests : $l = 15.24$ cm (6.00 in.)

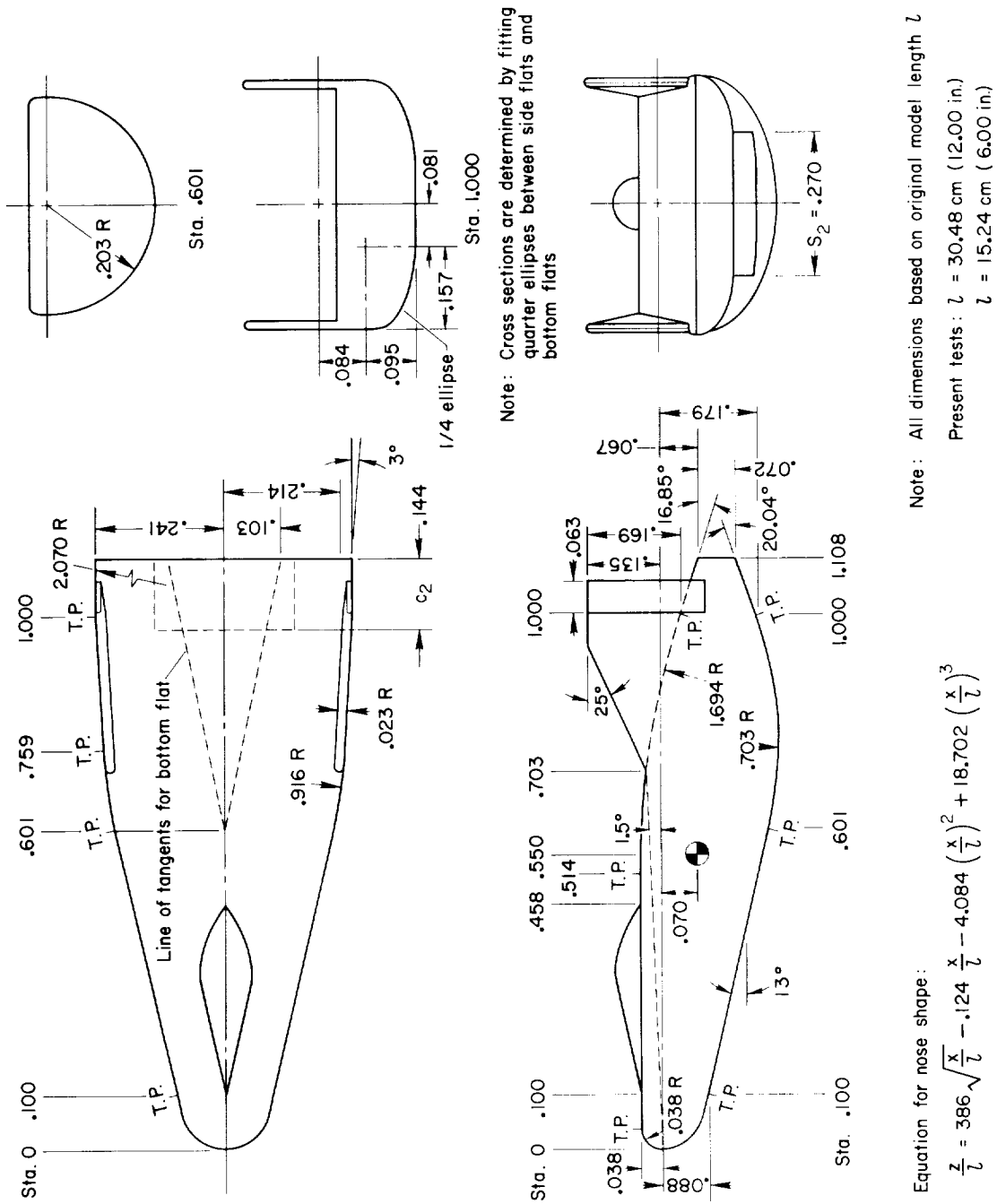
$l = 8.89$ cm (3.50 in.)

Equation for nose shape:

$$\frac{z}{l} = 386 \sqrt{\frac{x}{l}} - .124 \frac{x}{l} - 4.084 \left(\frac{x}{l}\right)^2 + 18.702 \left(\frac{x}{l}\right)^3$$

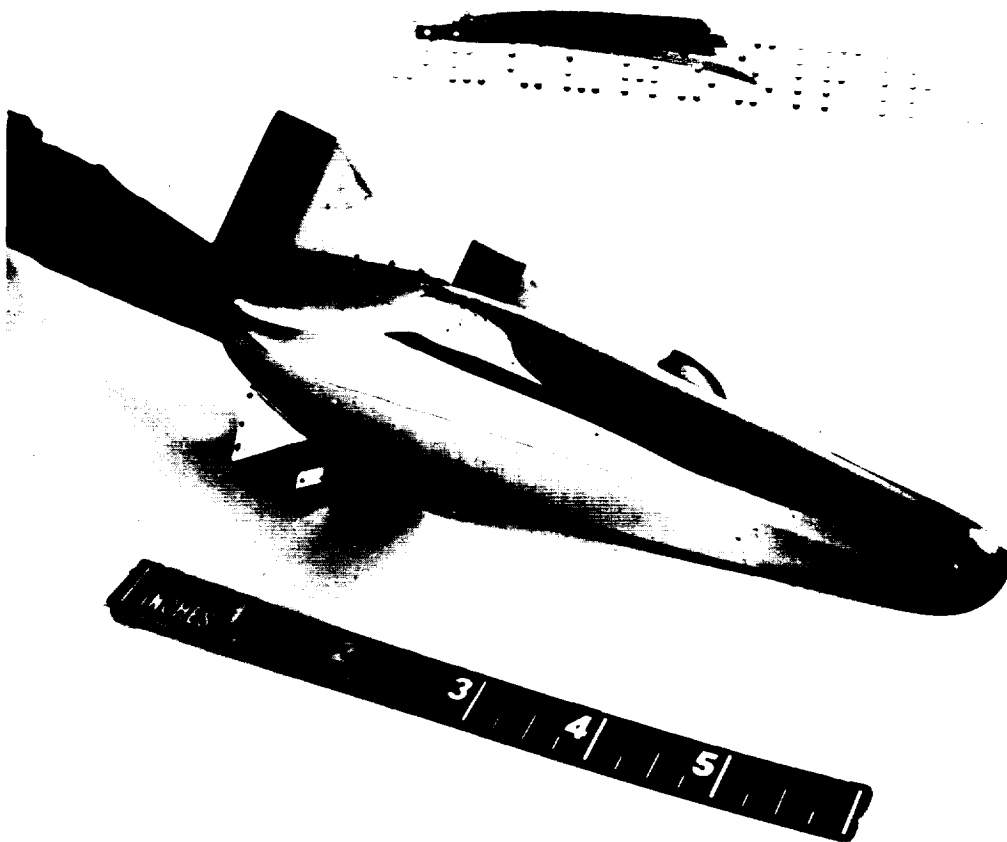
(a) M2 configuration.

Figure 1.- Model dimensions.



(b) M2-F2 configuration.

Figure 1.- Concluded.



(a) Low α M2 model.

A-40861



(b) High α M2 model.

A-40862

Figure 2.- Test models.



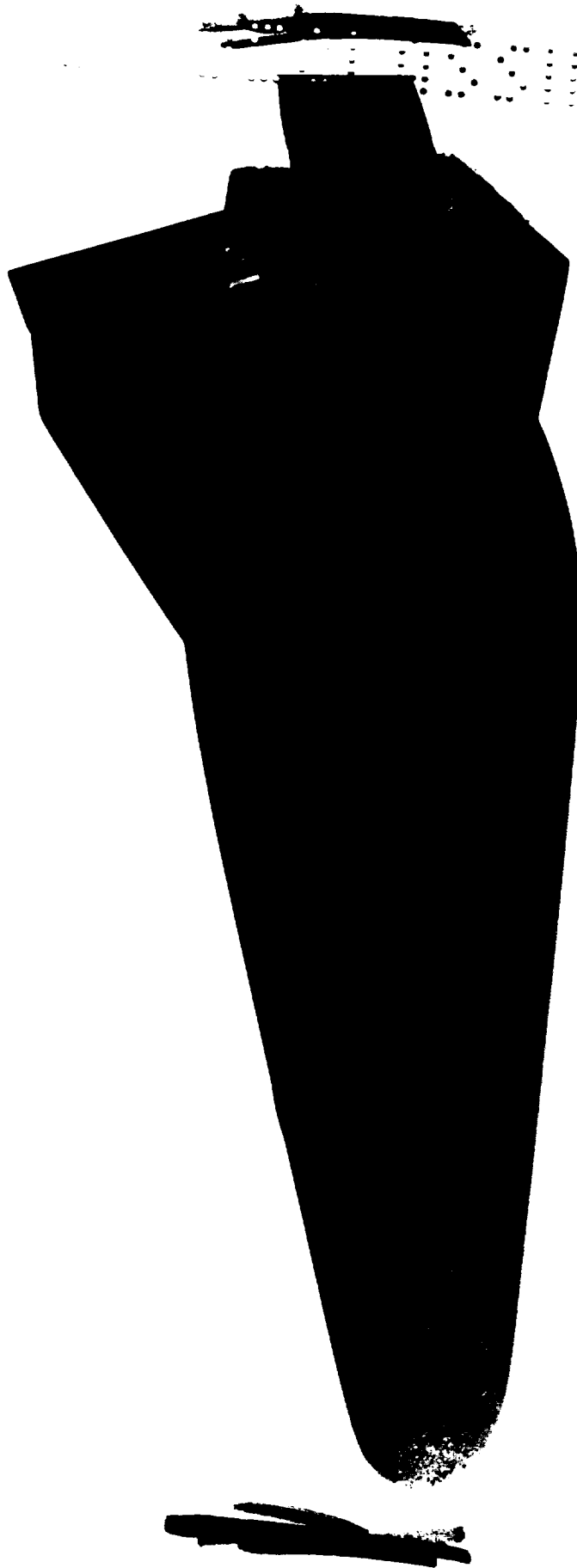


A35134

(c) M2-F2 model after thermal paint test in the shock tunnel; $\alpha = 0^\circ$, $\delta_p = 40^\circ$.

Figure 2.- Continued.

A-2292



(d) M2-F2 model after thermal paint test in the shock tunnel; $\alpha = 15^\circ$, $\beta = 15^\circ$, $\delta_p = 40^\circ$.

A-35239



A-30186

(e) M2 model during test in the shock tunnel; $\alpha = 0^\circ$, $\delta_p = 60^\circ$, $\delta_r = 35^\circ$.

Figure 2.- Concluded.

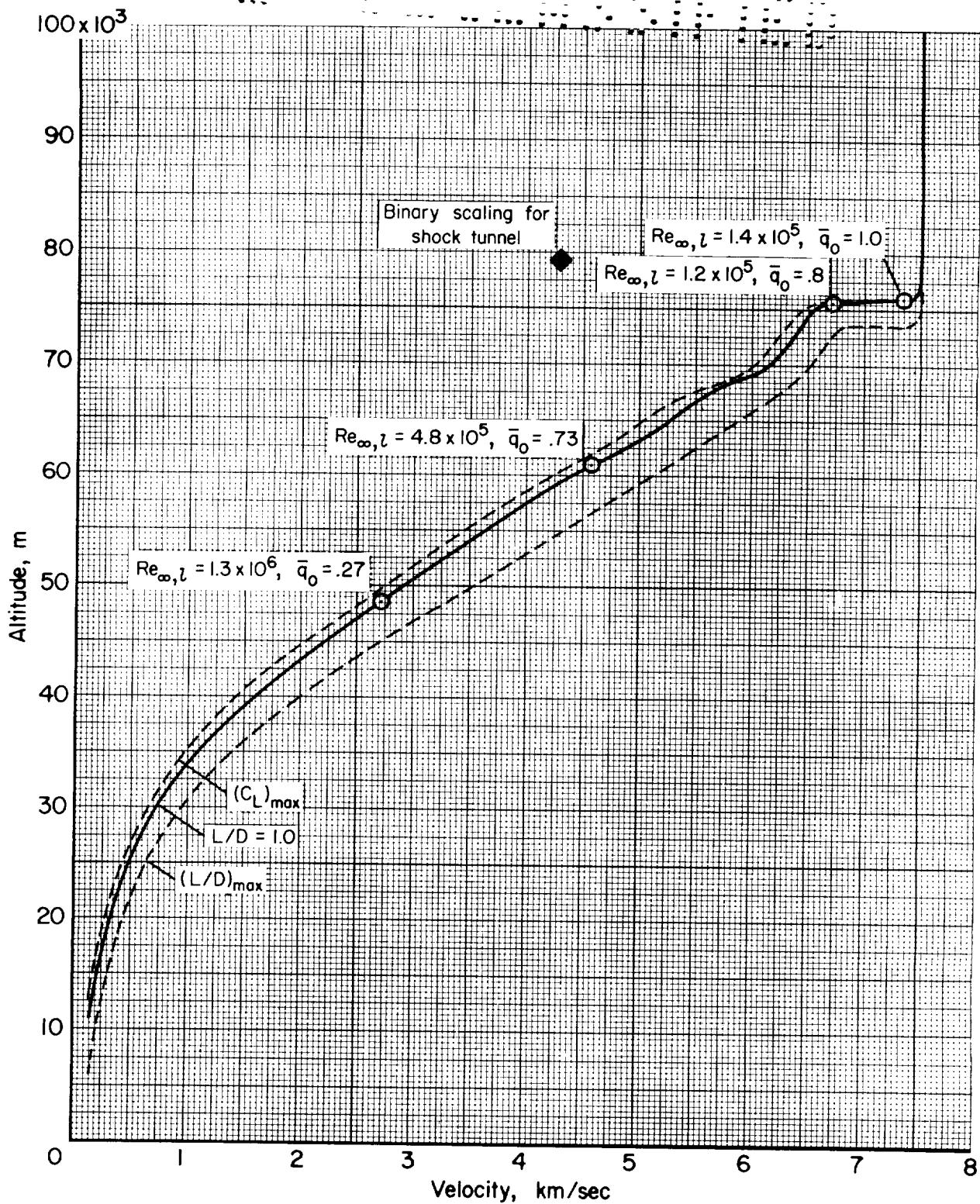


Figure 3.- M2-F2 nominal entry trajectories.

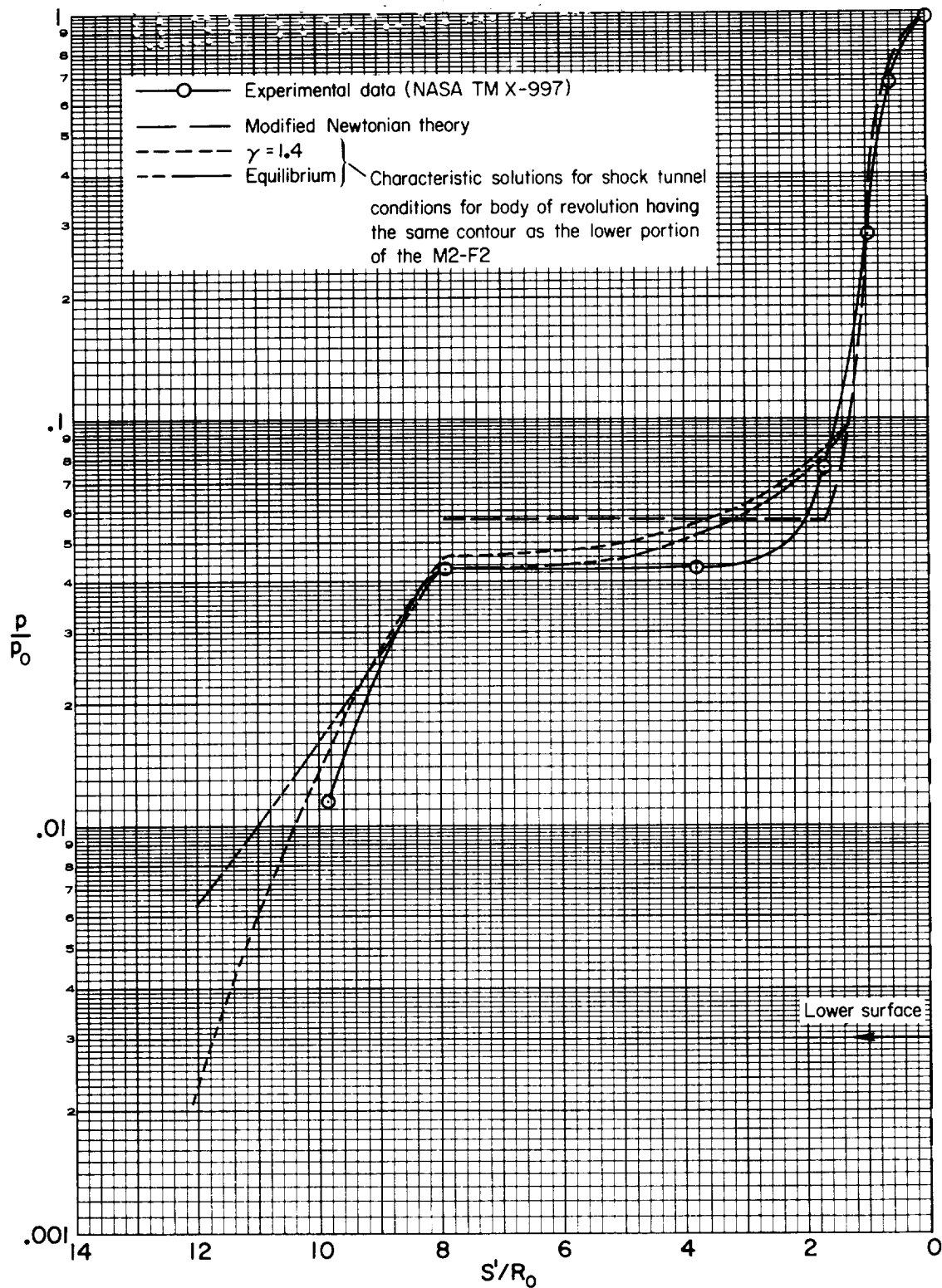
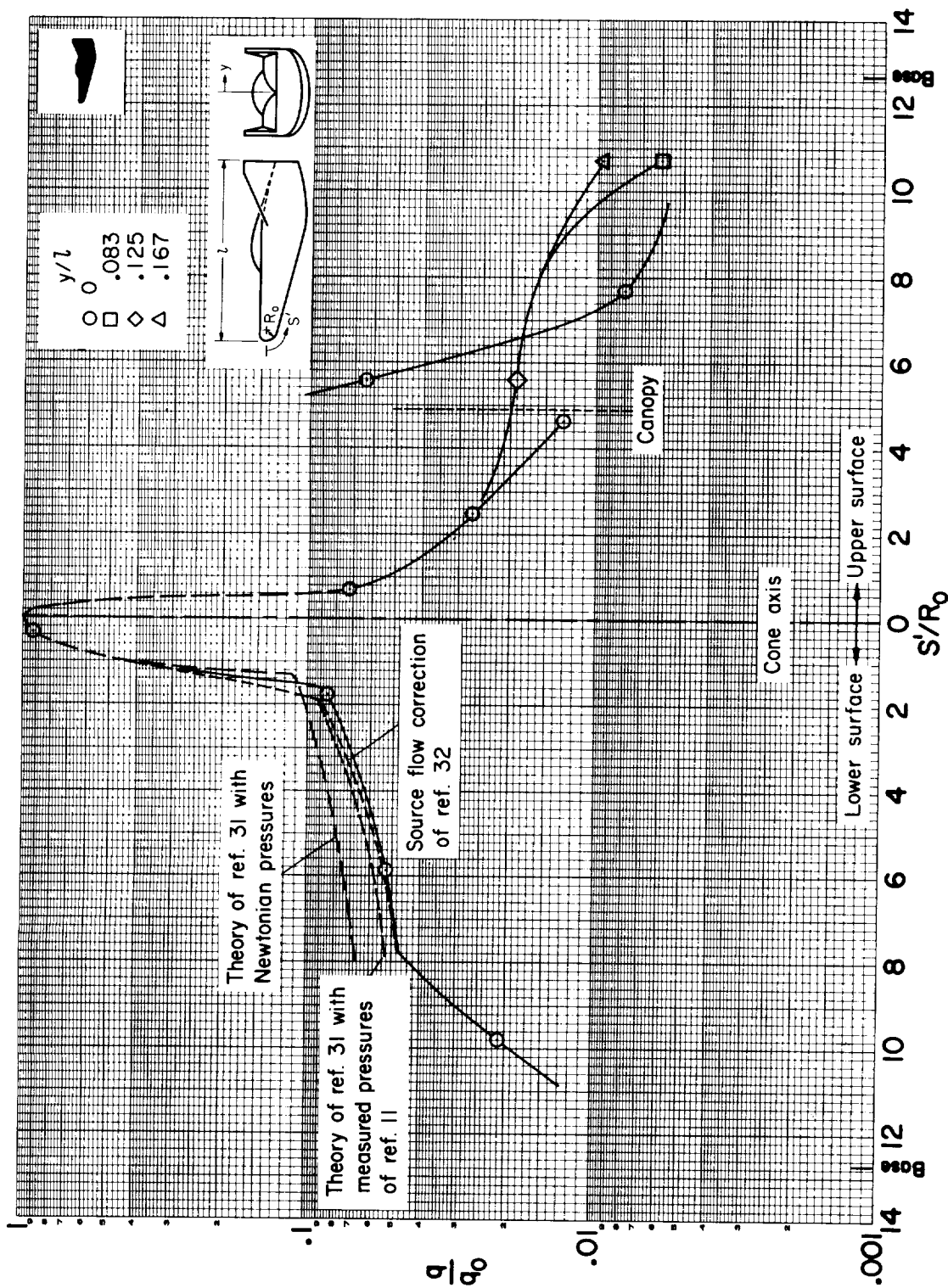
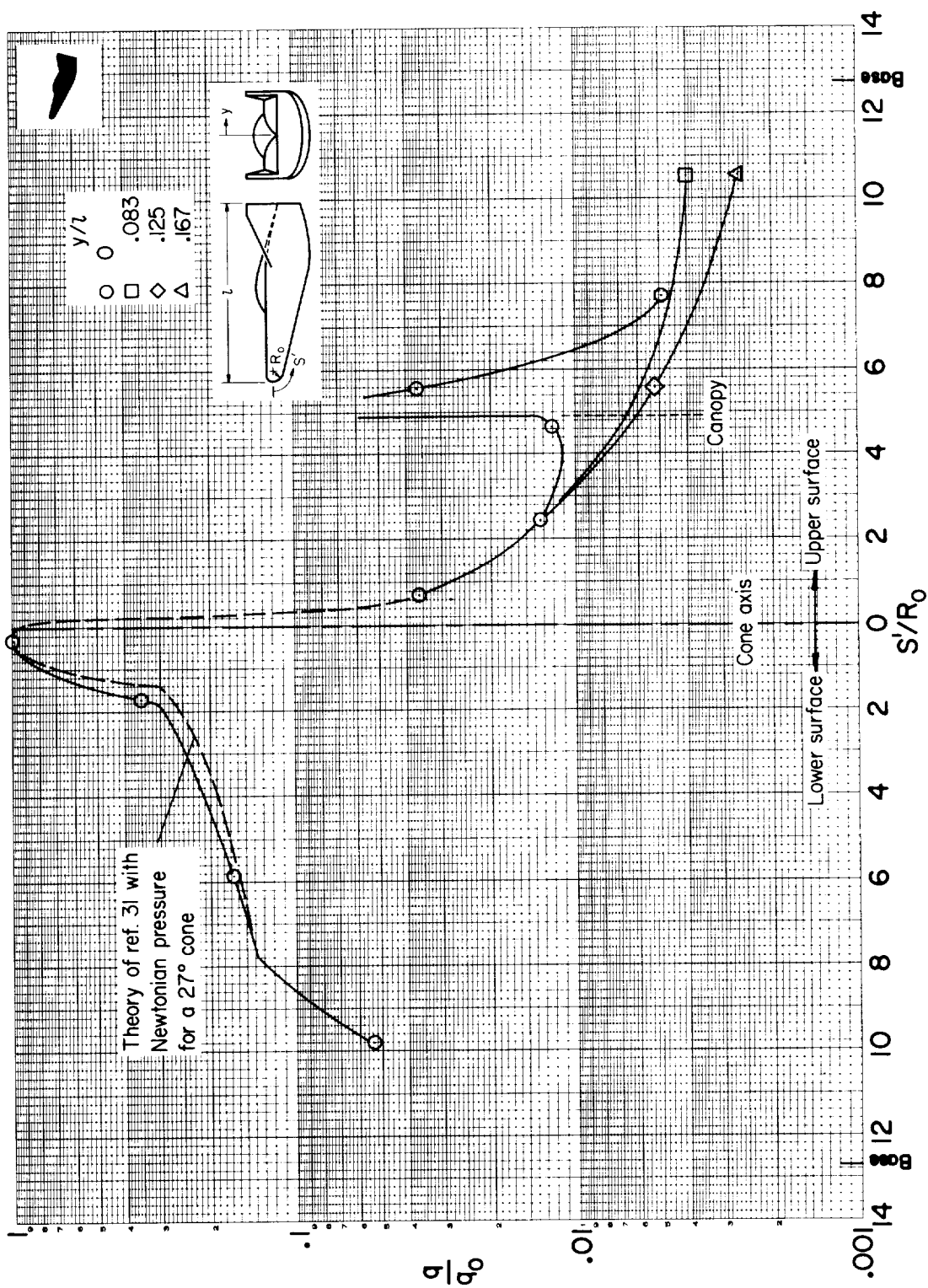


Figure 4.- Theoretical and experimental longitudinal surface pressure distributions for $\alpha = 0^\circ$.



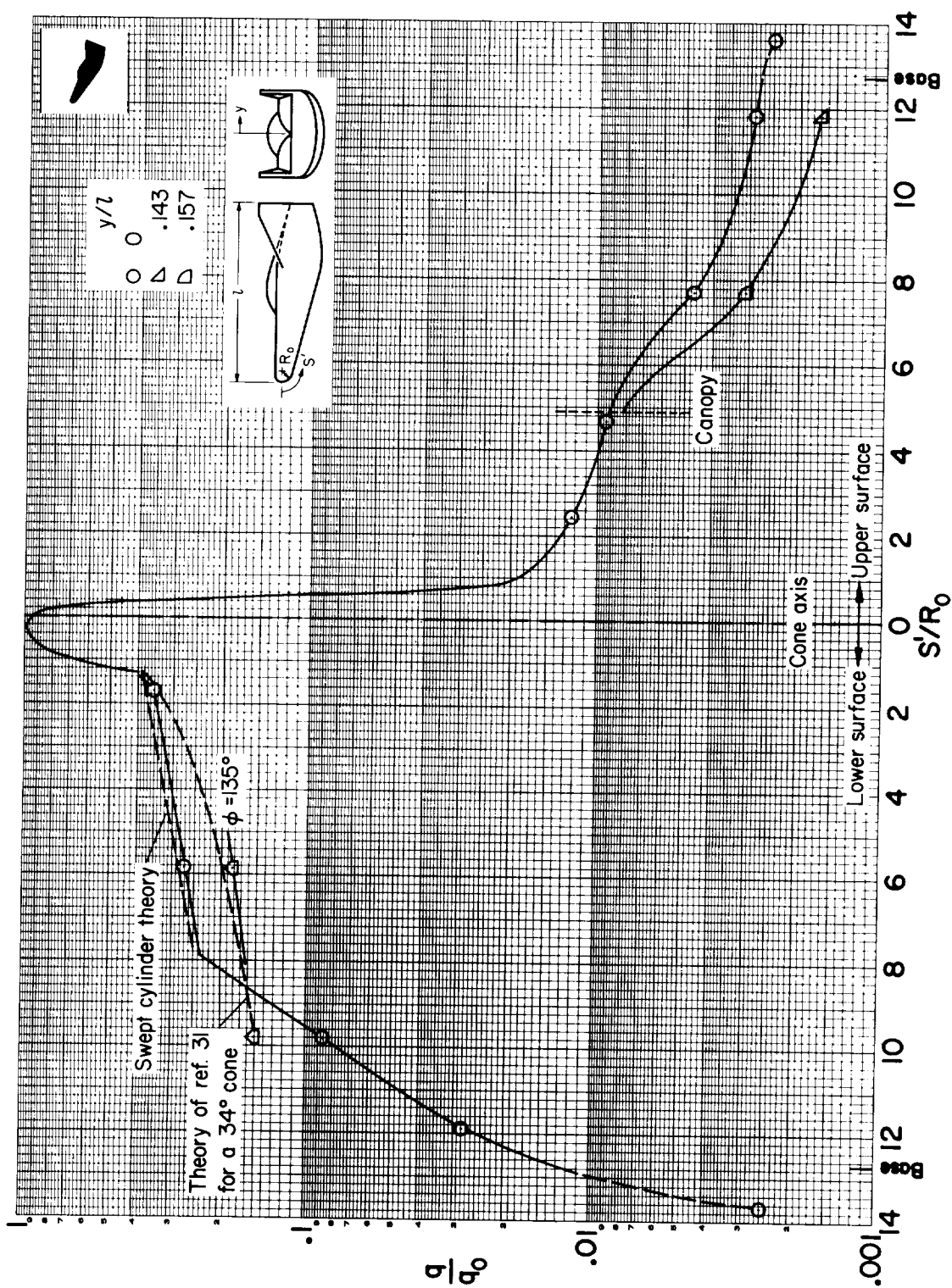
(a) $\alpha = 0^\circ$

Figure 5.- Longitudinal heating distributions for the M2 at $M_\infty = 10.0$.



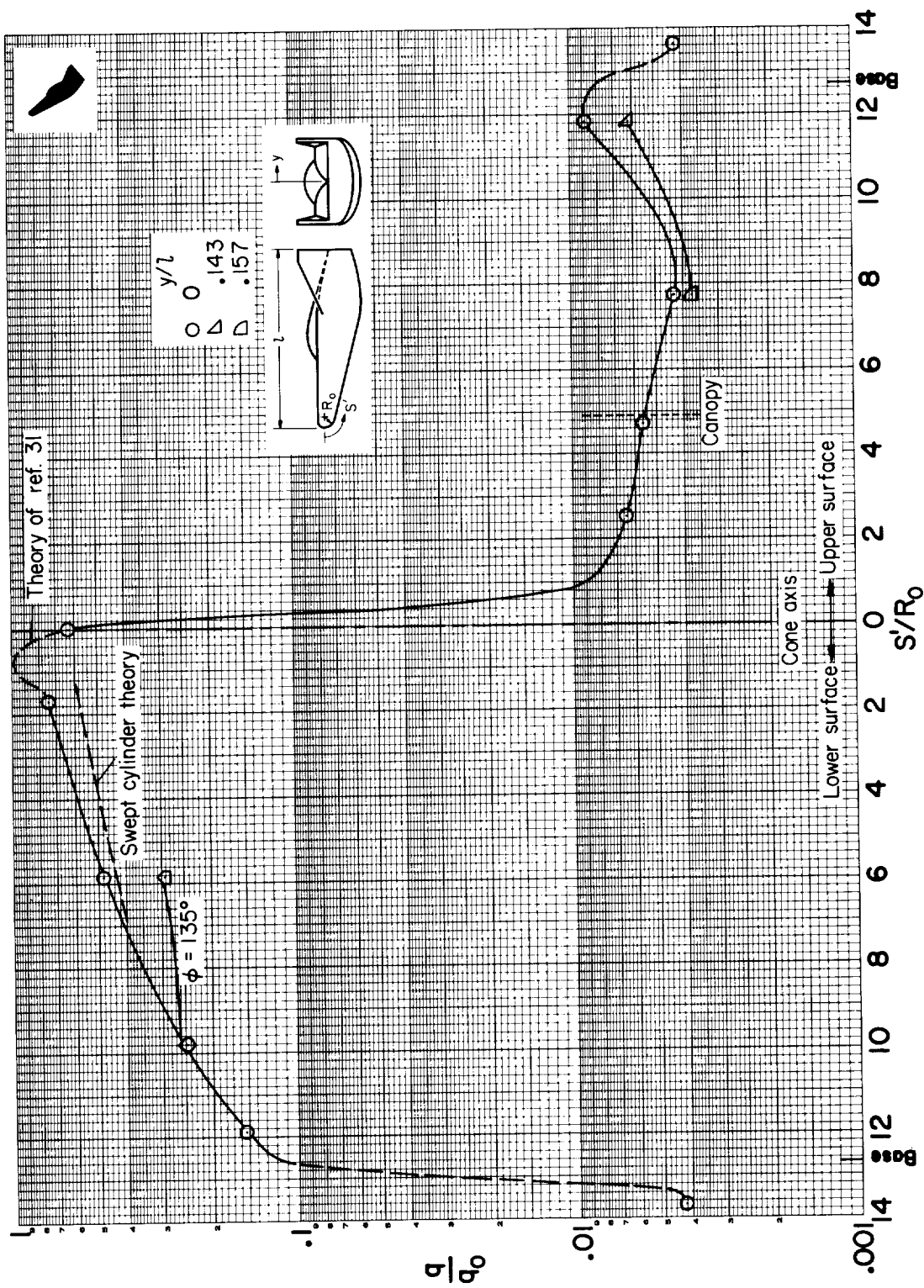
(b) $\alpha = 14^\circ$

Figure 5.- Continued.



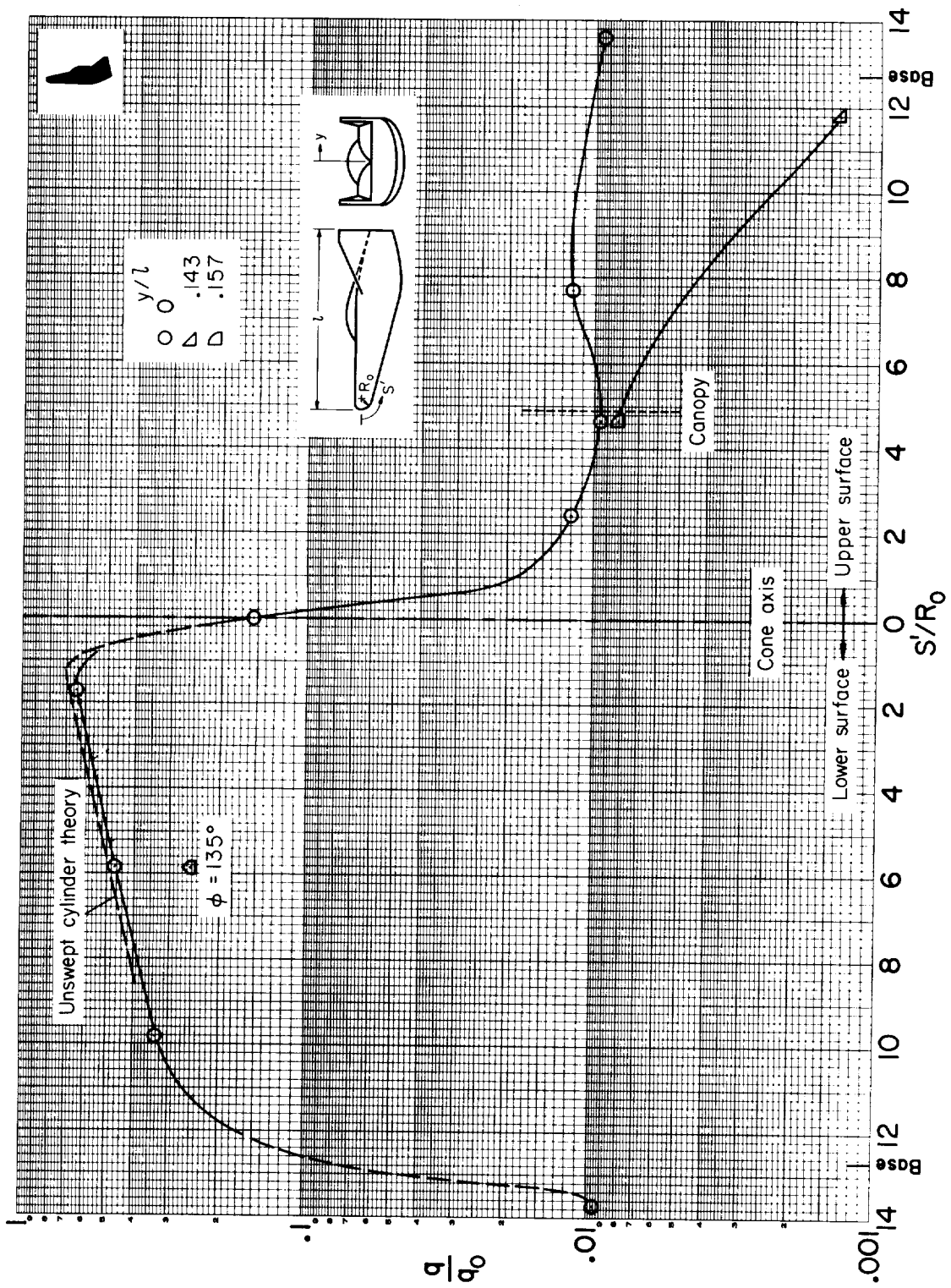
(c) $\alpha = 21^\circ$

Figure 5.- Continued.



(d) $\alpha = 49^\circ$

Figure 5.- Continued.



(e) $\alpha = 77^\circ$

Figure 5.- Concluded.

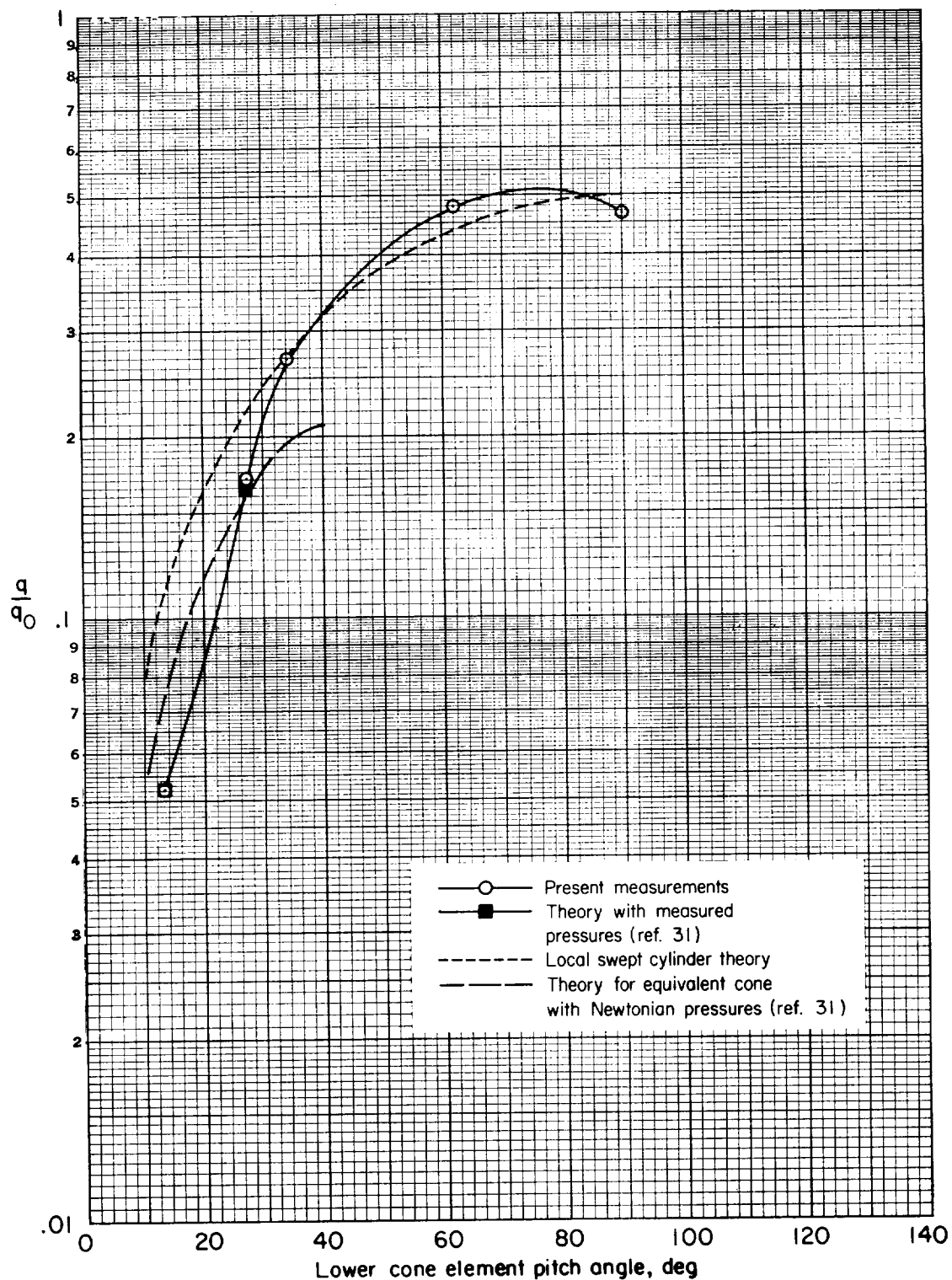
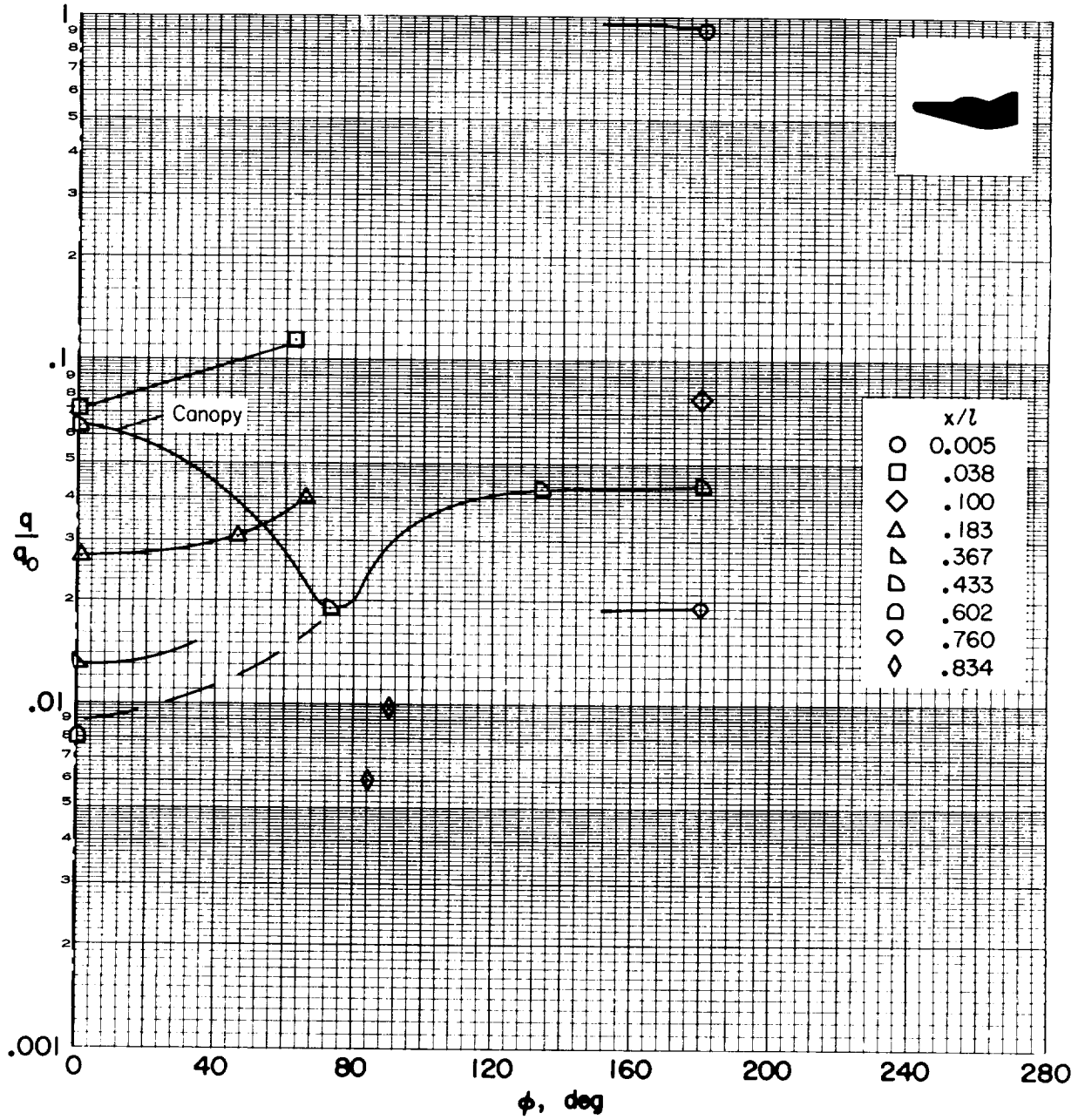
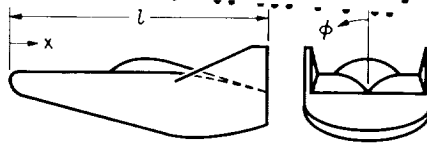
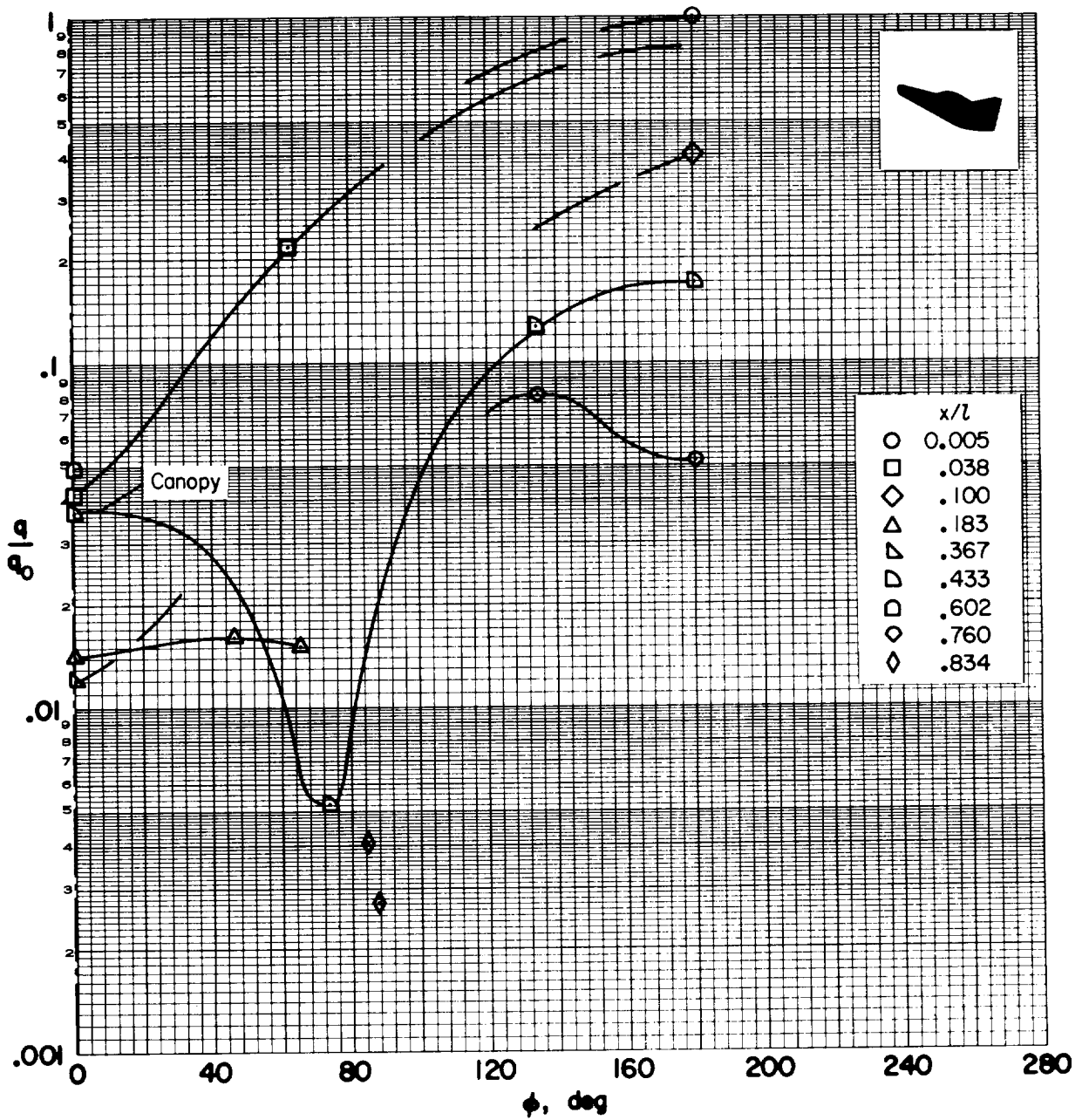
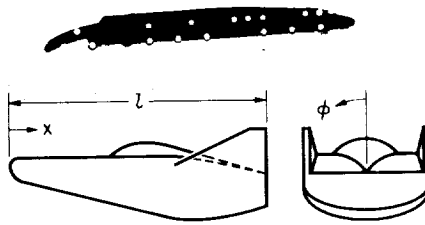


Figure 6.- Heating of the conical portion of the M2 for various angles of attack (at $S'/R_0 = 5.84$, $M_\infty = 10$).



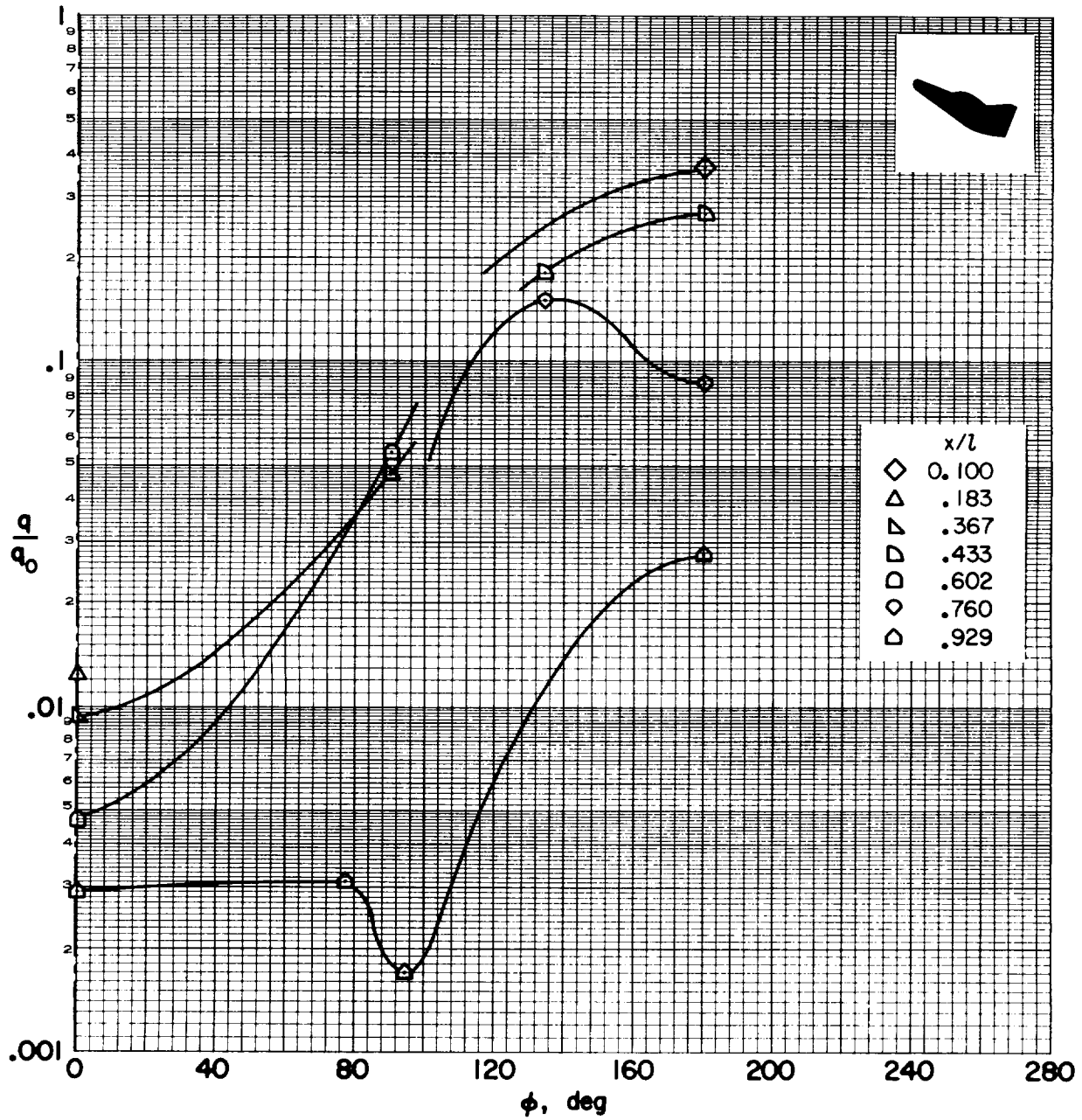
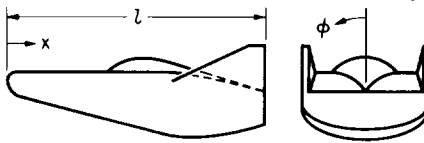
(a) $\alpha = 0^\circ$

Figure 7.- Circumferential heating of the M2 for several angles of attack at $M_\infty = 10$.



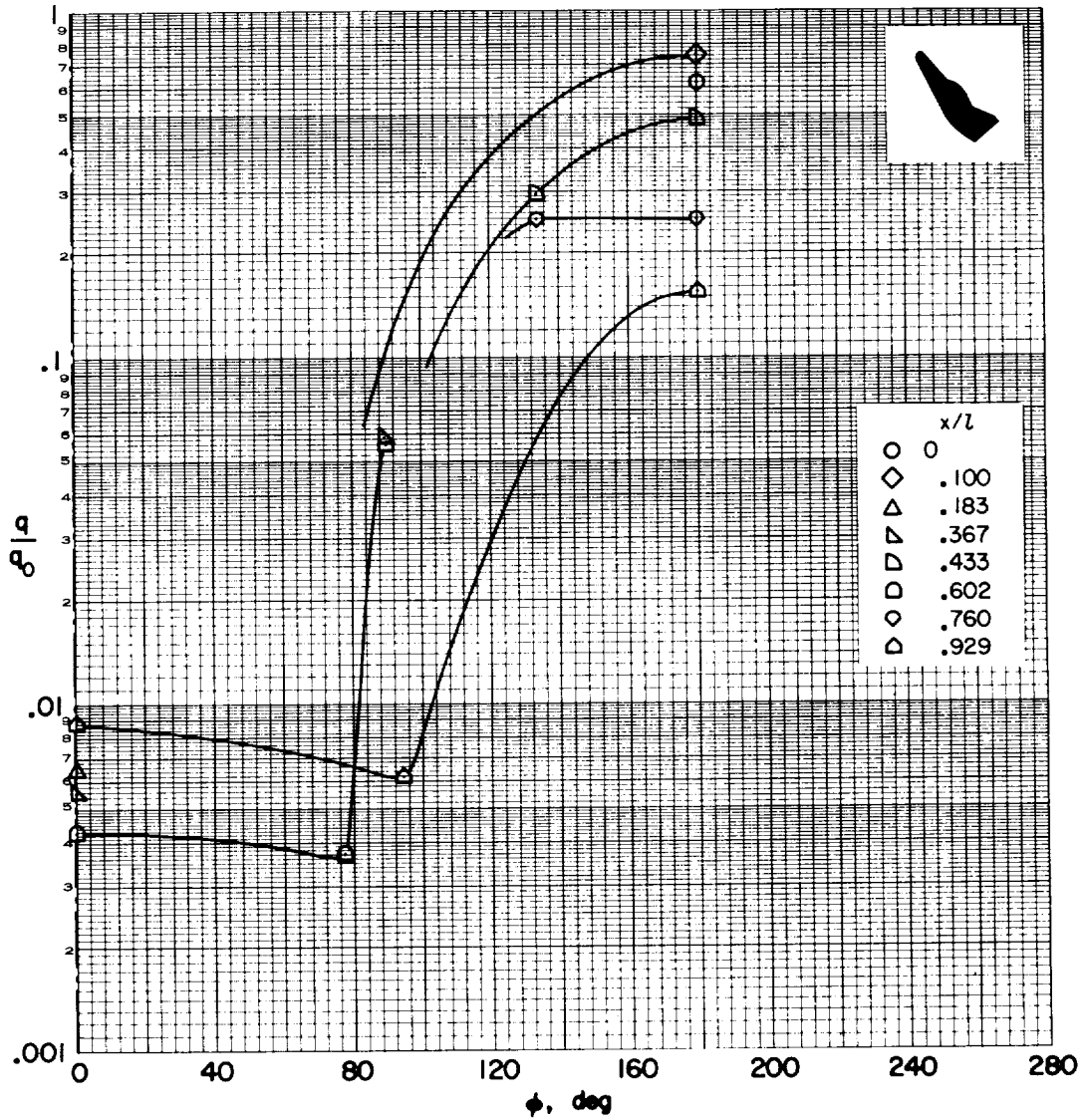
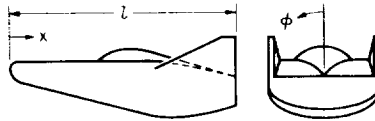
(b) $\alpha = 14^\circ$

Figure 7.- Continued.



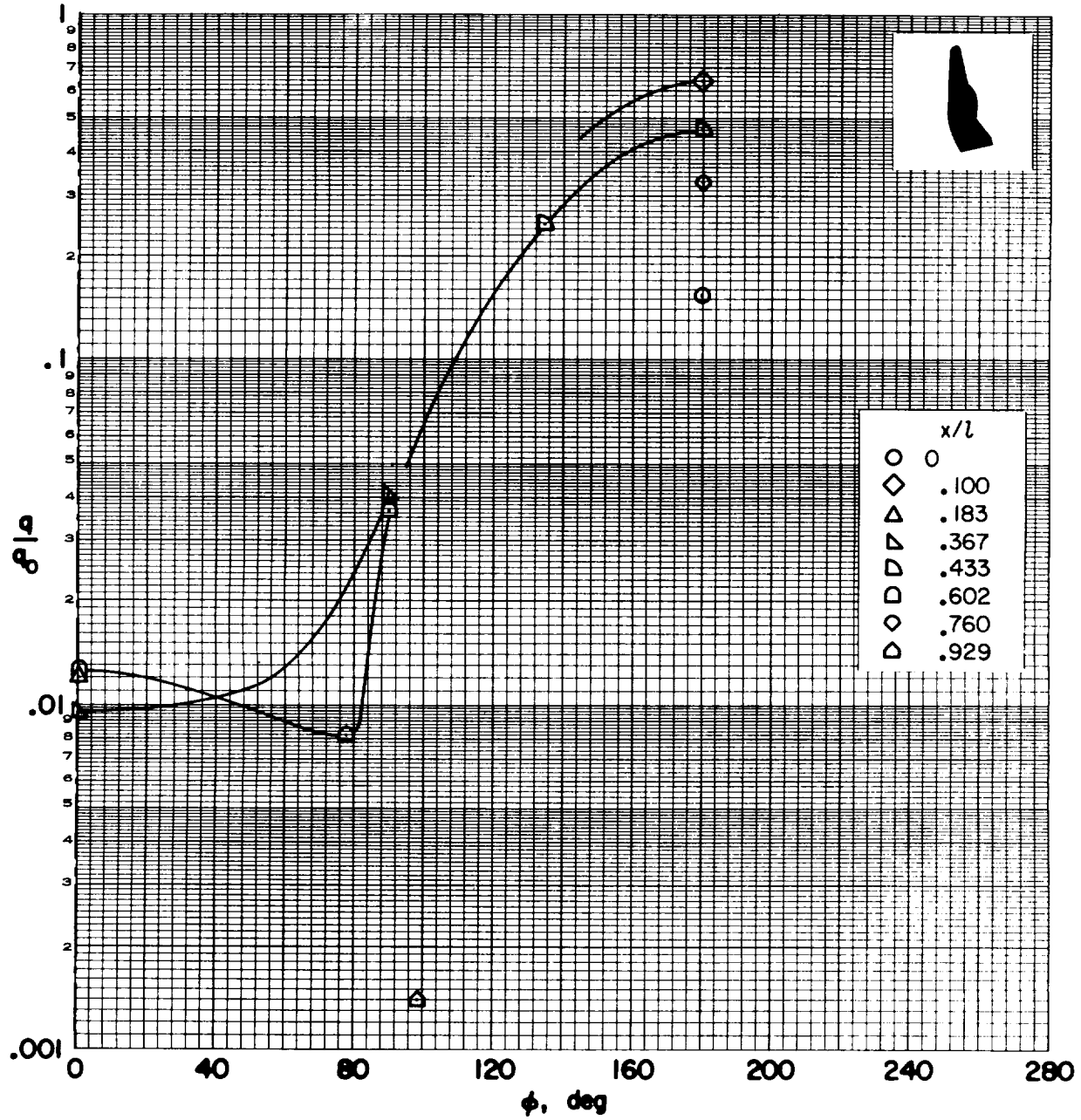
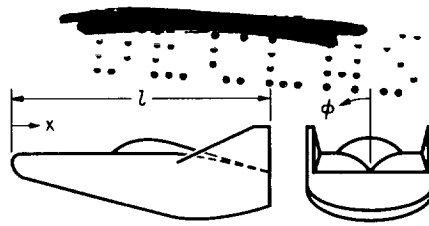
(c) $\alpha = 21^\circ$

Figure 7.- Continued.



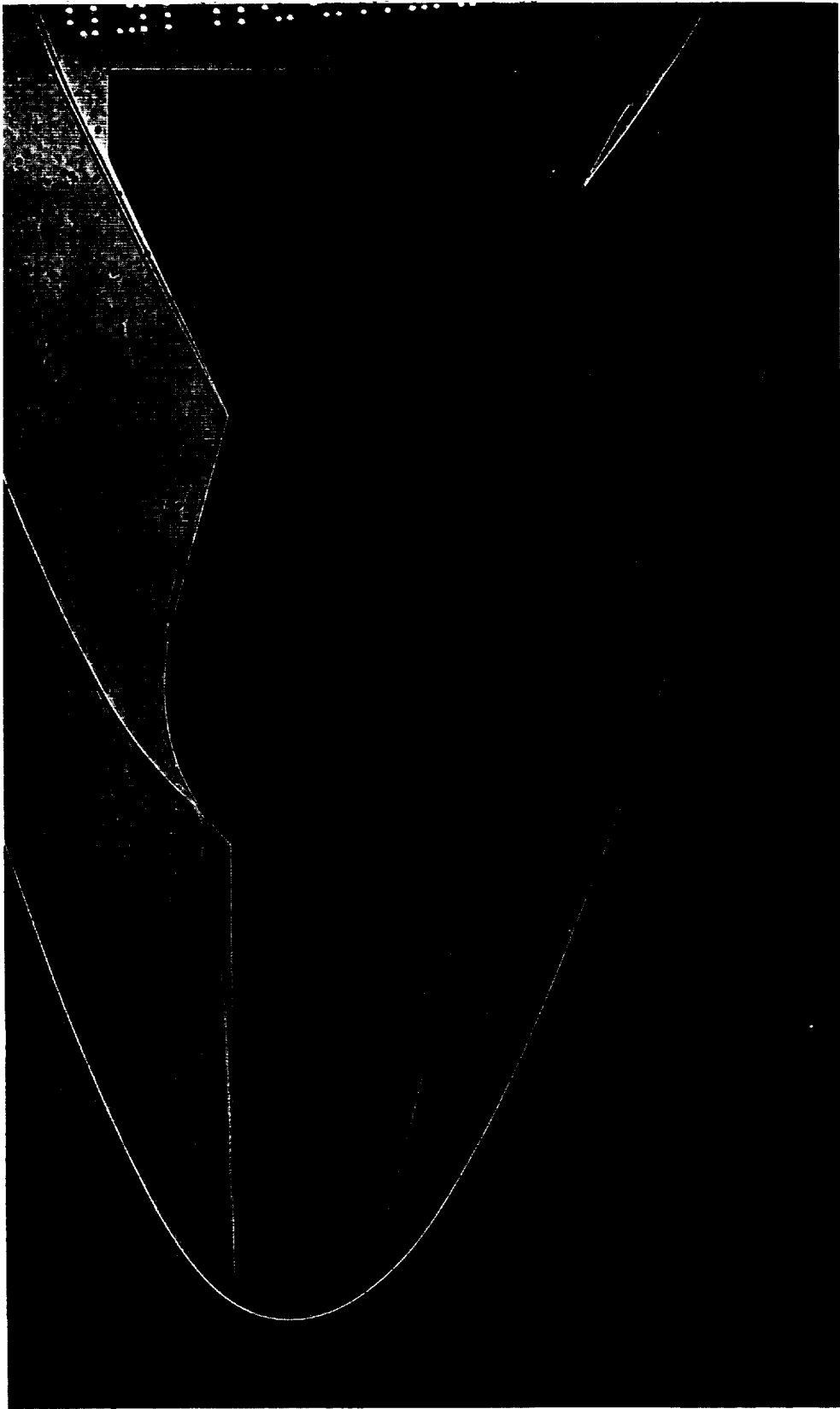
(d) $\alpha = 49^\circ$

Figure 7.- Continued.



(e) $\alpha = 77^\circ$

Figure 7.- Concluded.



A-40865

(a) $\alpha = 0^\circ$, $\delta_p = 45^\circ$, $M_\infty = 5$, $Re_\infty, l = 1.9 \times 10^6$, $T_w/T_s \approx 0.7$, 10- by 14-inch tunnel.

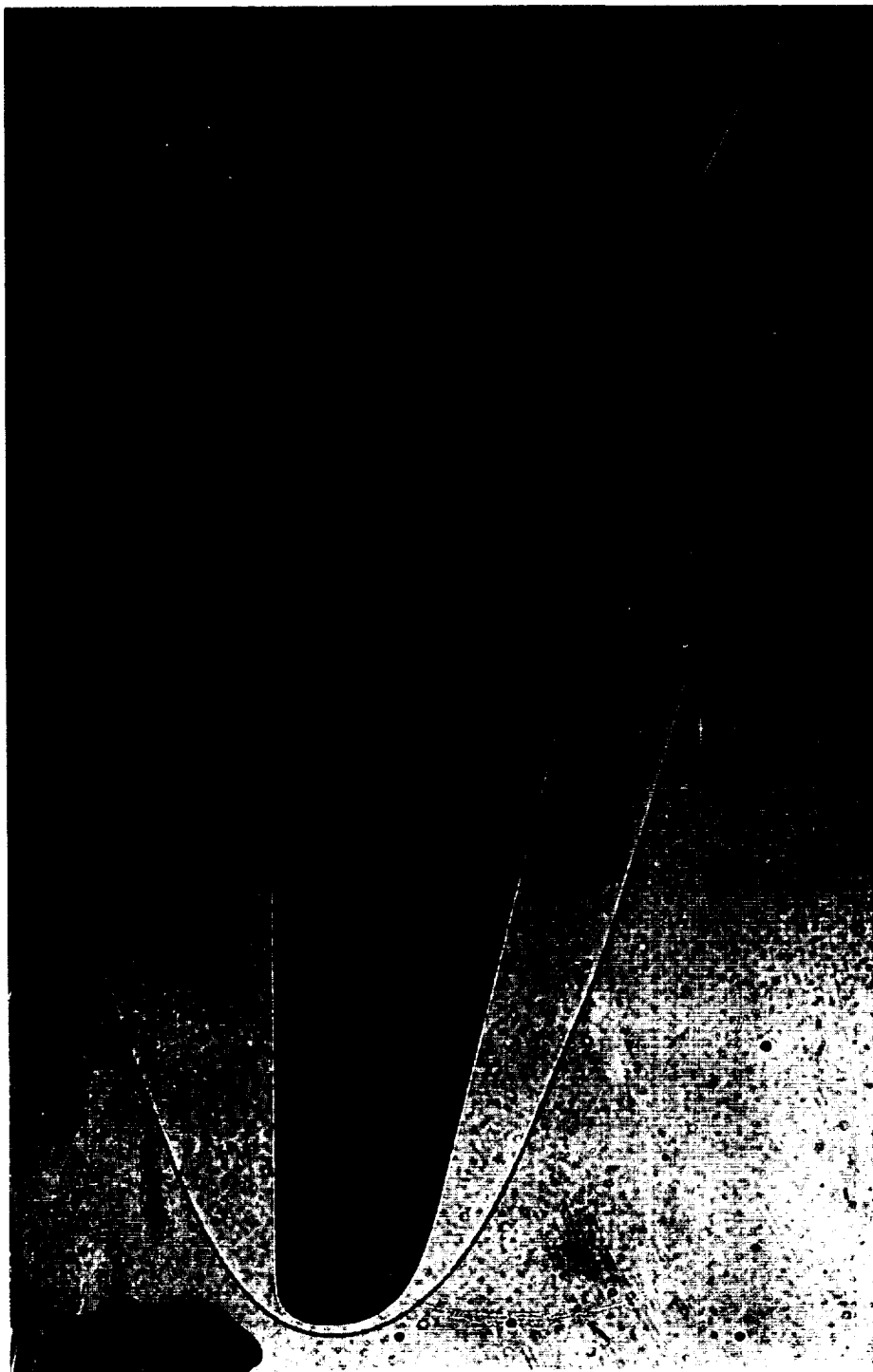
Figure 8.- Shadowgraphs of the flow about the M2.



A-486

(b) $\alpha = 14^\circ$, $\delta_p = 45^\circ$, $M_\infty = 5$, $Re_\infty, \lambda = 1.9 \times 10^6$, $T_w/T_s \approx 0.7$, 10- by 1-inch tunnel.

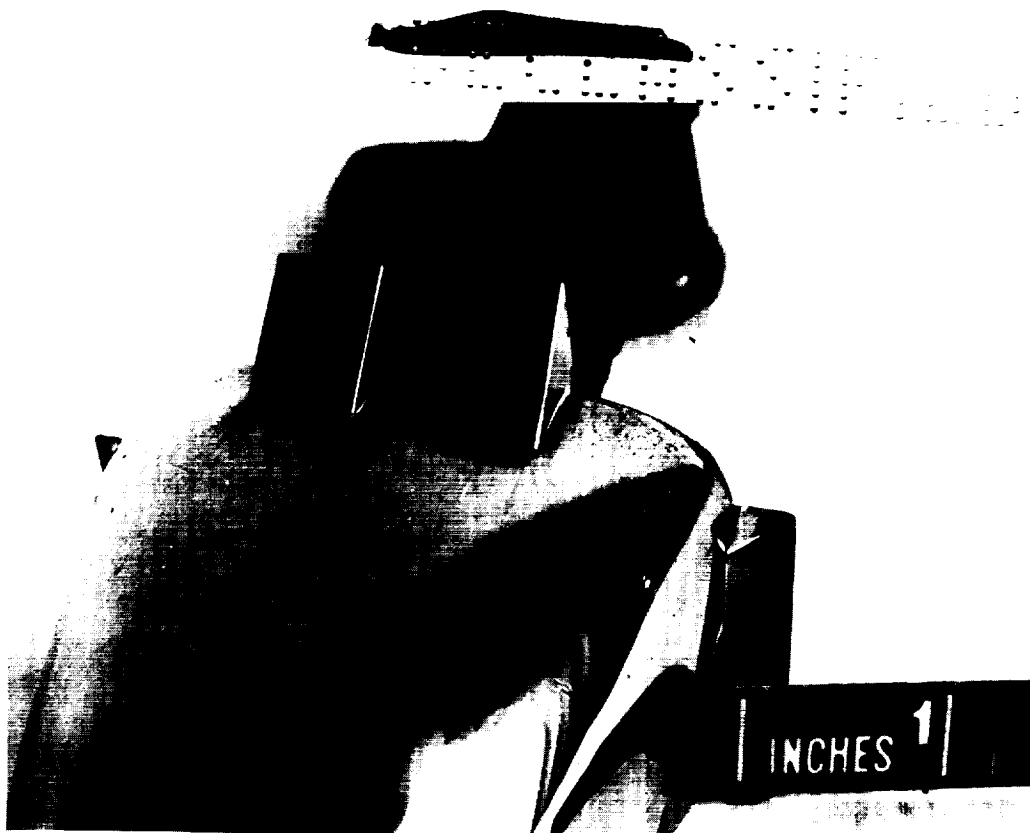
Figure 8.- Continued.



A40866

(c) $\alpha = 0^\circ$, $\delta_p = 45^\circ$, $M_\infty = 10.4$, $Re_{\infty, l} = 0.55 \times 10^6$, $T_w/T_s \approx 0.63$, 3.5-foot tunnel.

Figure 8.- Concluded.



(a) Front view of body and controls.

A-40863



(b) Rear view.

A-40864

Figure 9.- Photographs of the M2 model after test in the 1-foot shock tunnel
at $M_{\infty} = 10$; $\alpha = 14^{\circ}$, $\delta_p = 45^{\circ}$, $\delta_r = 35^{\circ}$.

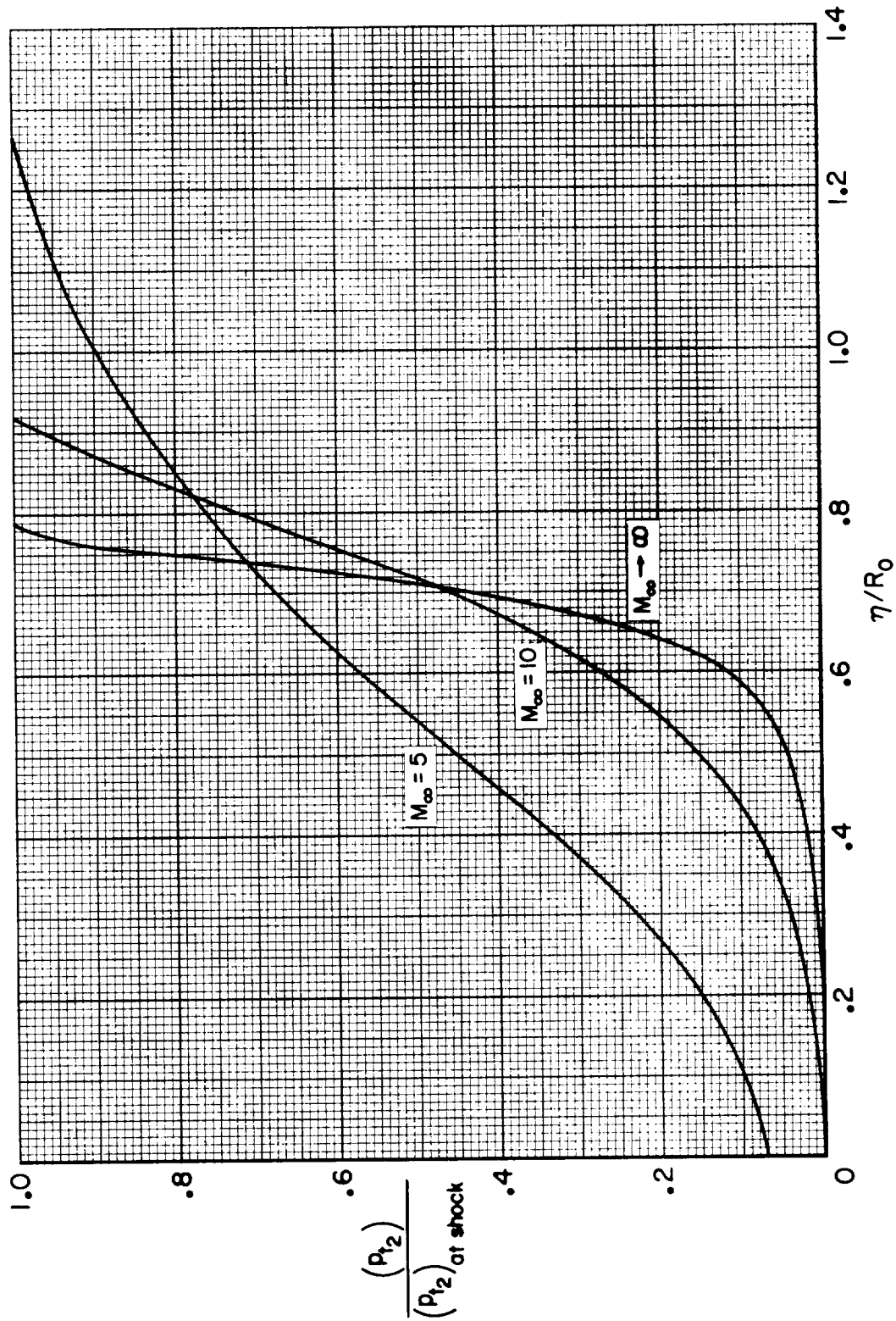
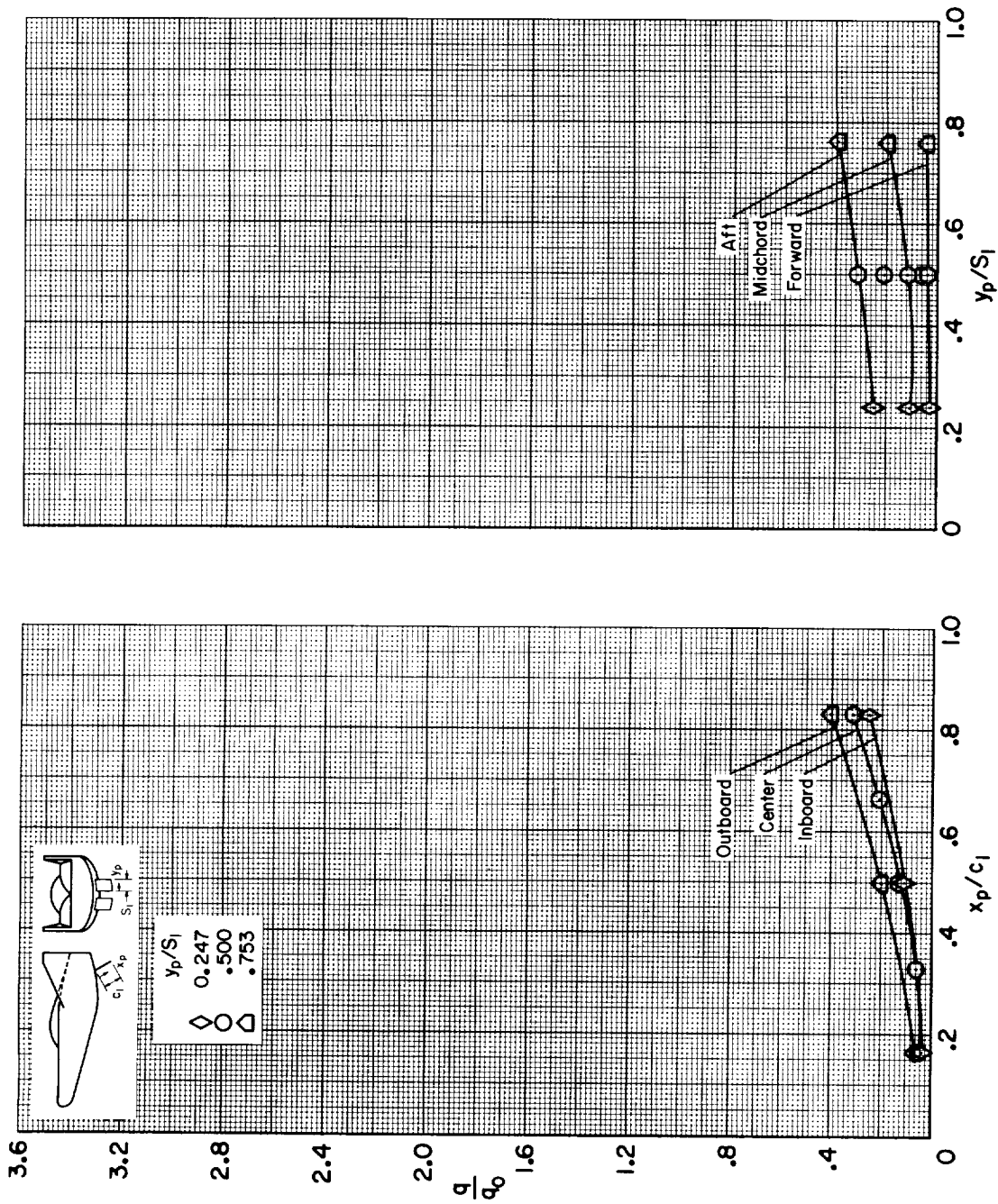
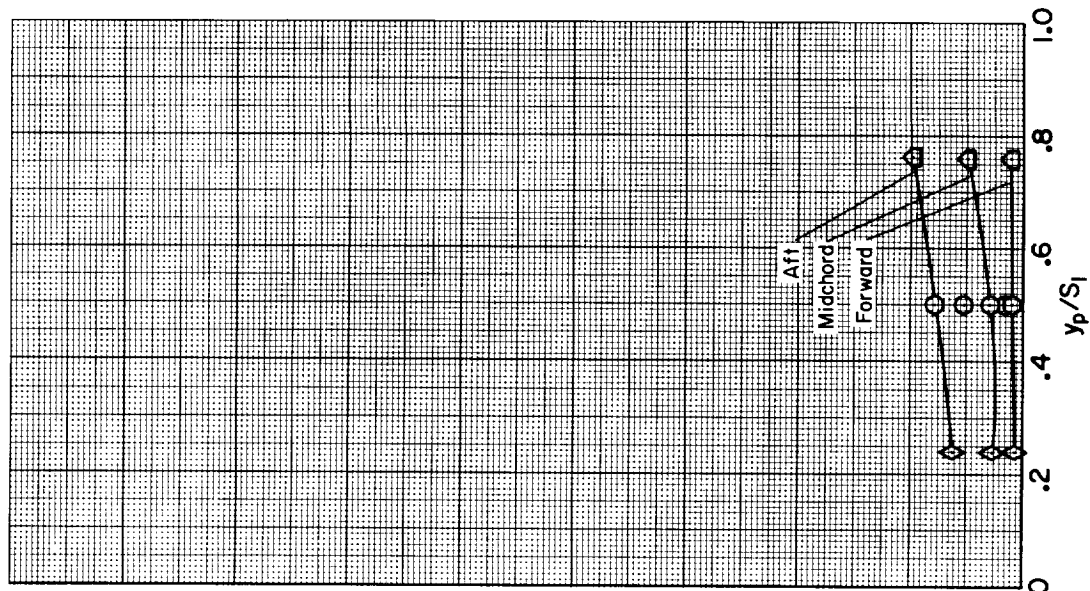


Figure 10.- Theoretical total-pressure distribution at $x/R_0 = 5.0$ in the inviscid flow about a blunted 15° cone for several Mach numbers.

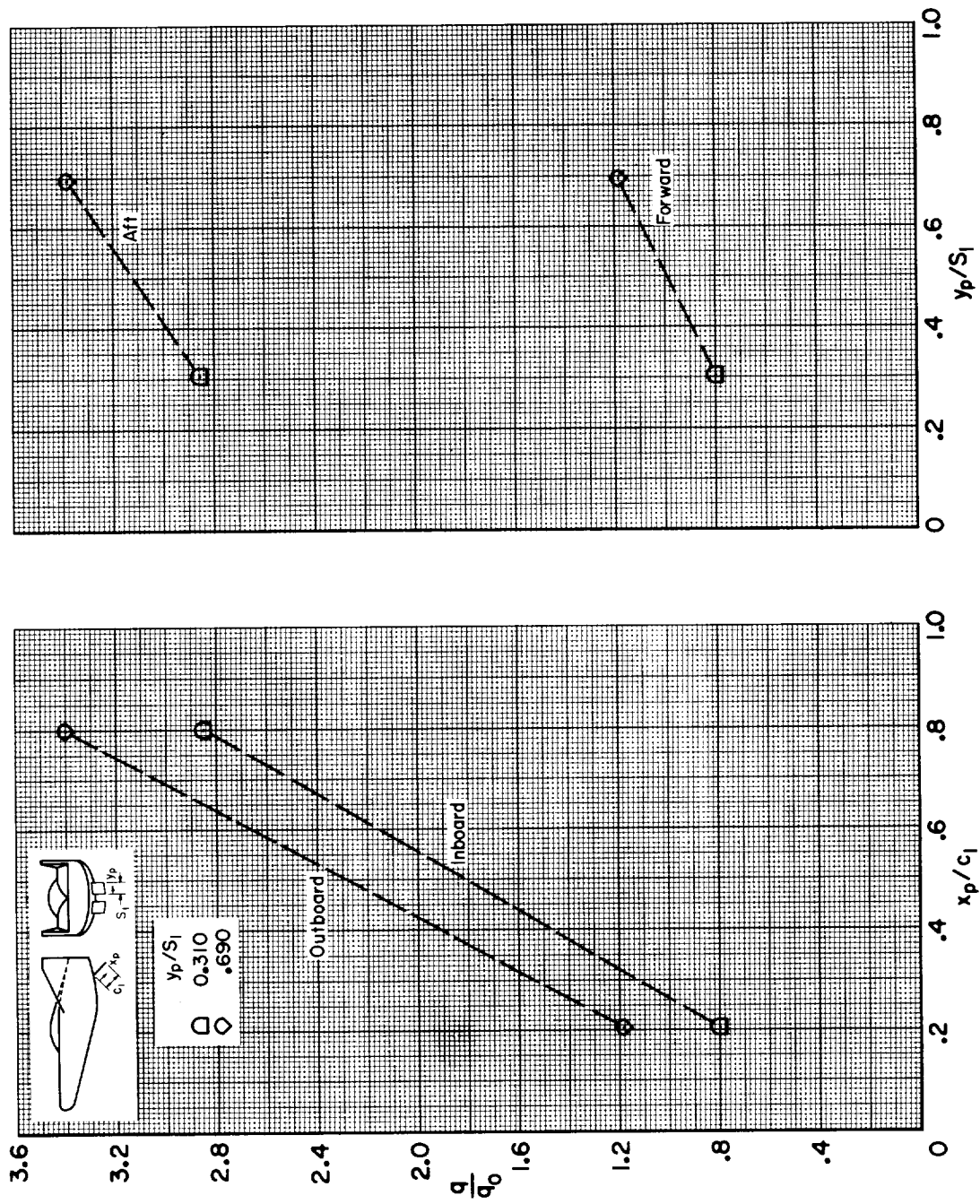


(a) Longitudinal.



(b) Spanwise.

Figure 11.- Heat transfer to the pitch controls of the M2 for $\alpha = 0^\circ$; $\delta_p = 60^\circ$, $M_\infty = 10$.



(b) Spanwise.

(a) Longitudinal.

Figure 12.- Heat transfer to the pitch controls of the M2 for $\alpha = 14^\circ$; $\delta_p = 45^\circ$, $M_\infty = 10$.

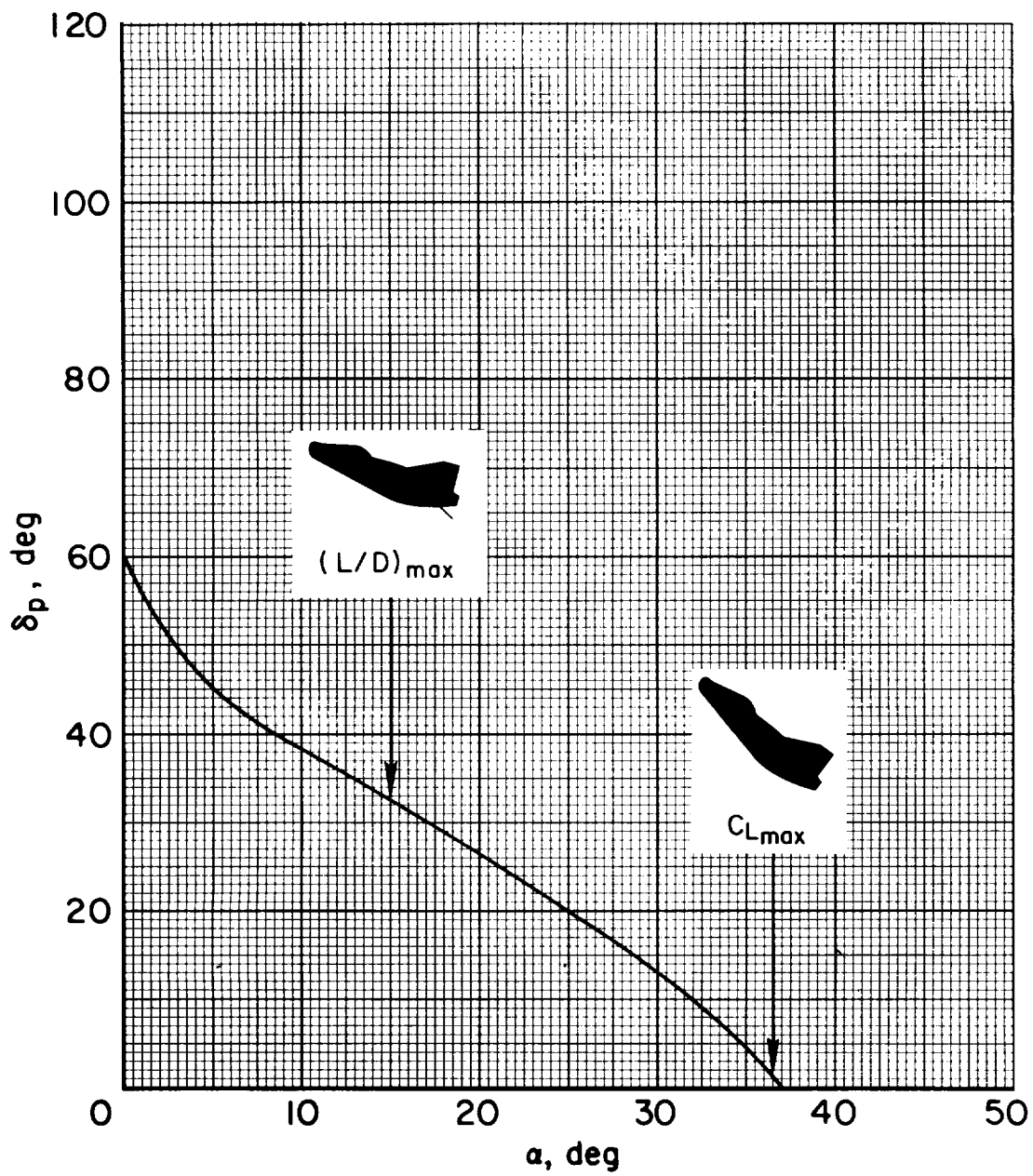
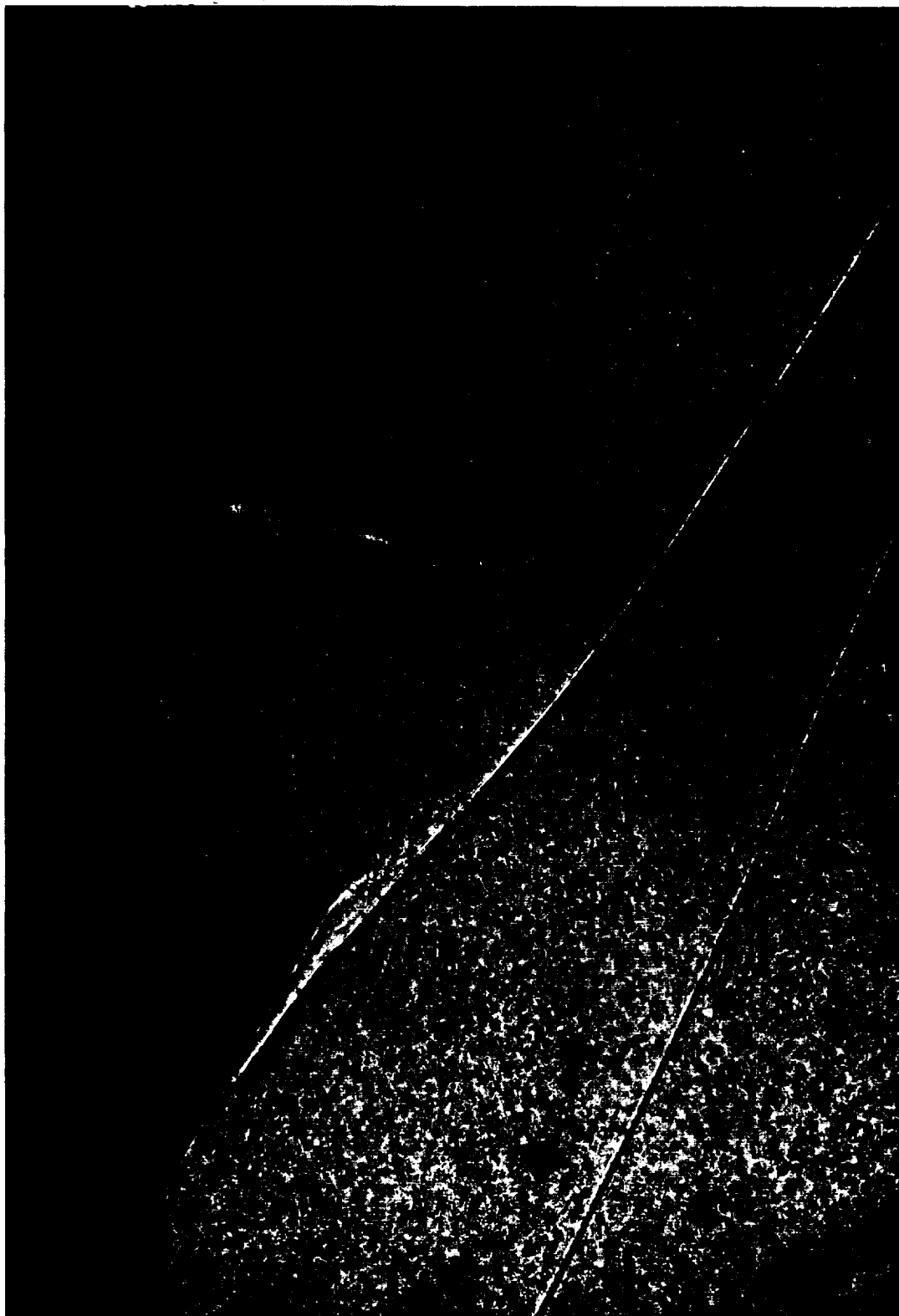


Figure 13.- Pitch control deflection required for longitudinal trim of the M2-F2.



A-40867

(a) $M_{\infty} = 5.2$, $Re_{\infty, l} = 0.85 \times 10^6$, $\alpha = 15^\circ$, $\delta_p = 35^\circ$

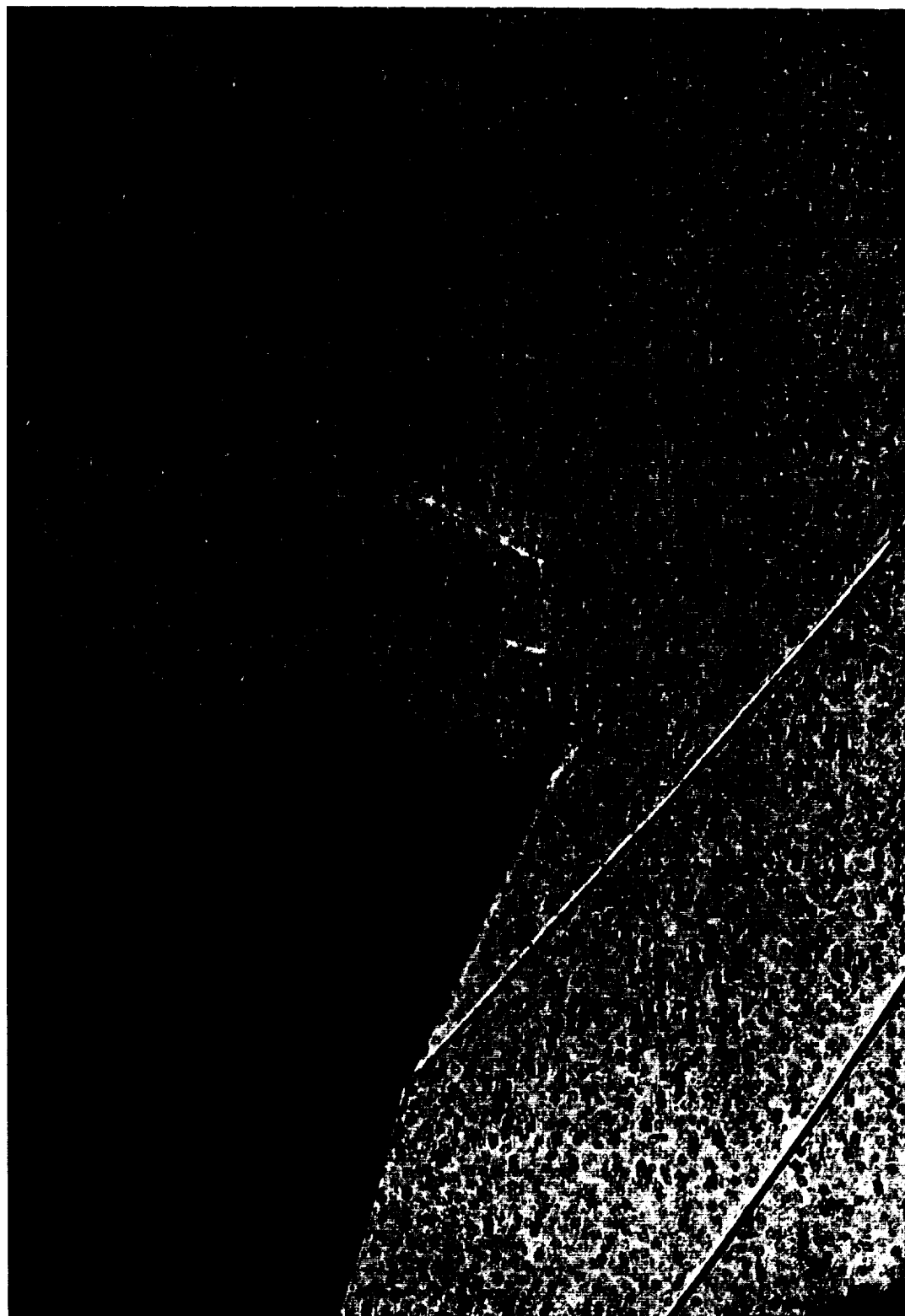
Figure 14.- Shadowgraphs of the flow over the pitch controls of the M2-F2 model in the 3.5-foot tunnel.



(b) $M_\infty = 10.4$, $Re_\infty, \gamma = 1.07 \times 10^6$, $\alpha = 15^\circ$, $\delta_p = 35^\circ$

Figure 14.- Continued.

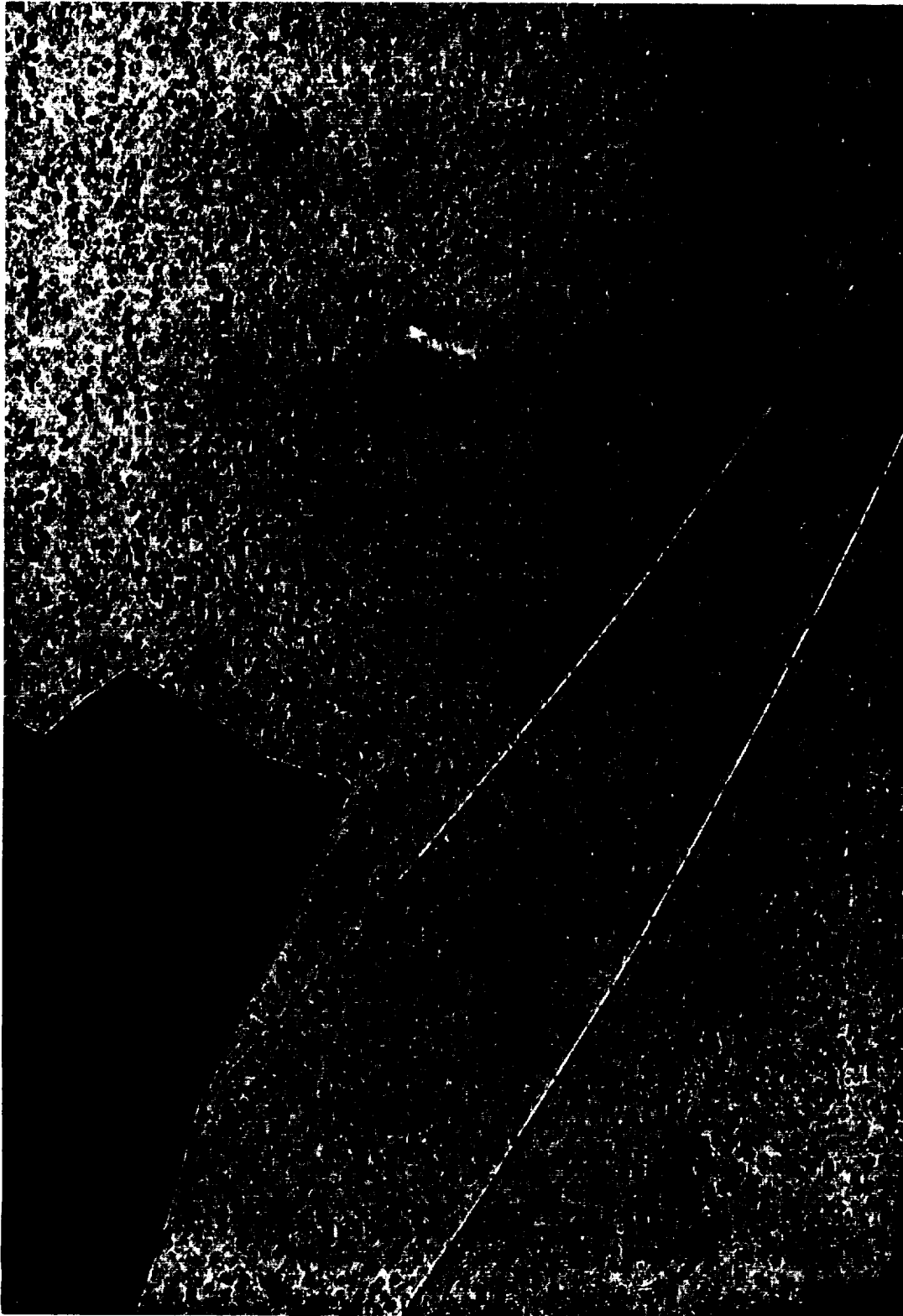
A-40868



A-40869

(c) $M_{\infty} = 5.2$, $Re_{\infty} \lambda = 0.85 \times 10^6$, $\alpha = 30^\circ$, $\delta_p = 15^\circ$

Figure 14.- Continued.



A-40870

(d) $M_c = 10.11$, $Re_z = 1.07 \times 10^6$, $\alpha = 30^\circ$, $\delta_p = 15^\circ$

Figure 14.- Concluded.



A-40858.1

(a) Self-luminous photograph; $M_\infty = 10$, $\alpha = 0^\circ$, $\delta_p = 40^\circ$.

Figure 15.- Flow-visualization photographs of the M2-F2 model tests in the shock tunnel.



A-40859.1

(b) Self-luminous photograph; $M_{\infty} = 10$, $\alpha = 15^{\circ}$, $\delta p = 40^{\circ}$.

Figure 15.- Continued.



A-40860.1

(c) Self-luminous photograph; $M_{\infty} = 10$, $\alpha = 15^{\circ}$, $\beta = 15^{\circ}$, $\delta_p = 40^{\circ}$.

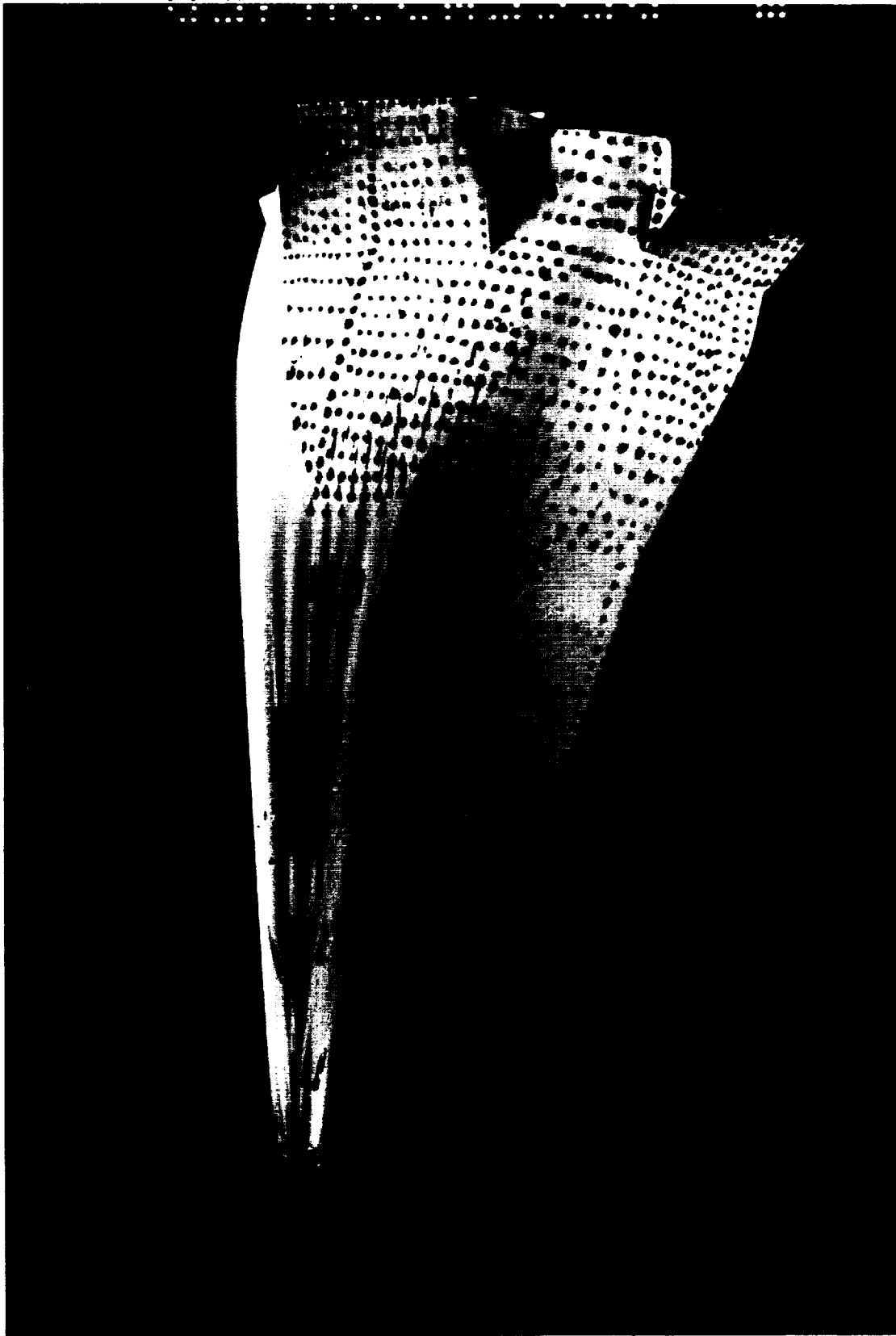
Figure 15.- Continued.



A-36322

(d) Appearance of thermal paint fringe patterns on the pitch control after test at $M_o = 1.4$; $\alpha = 15^\circ$, $\delta_p = 40^\circ$.

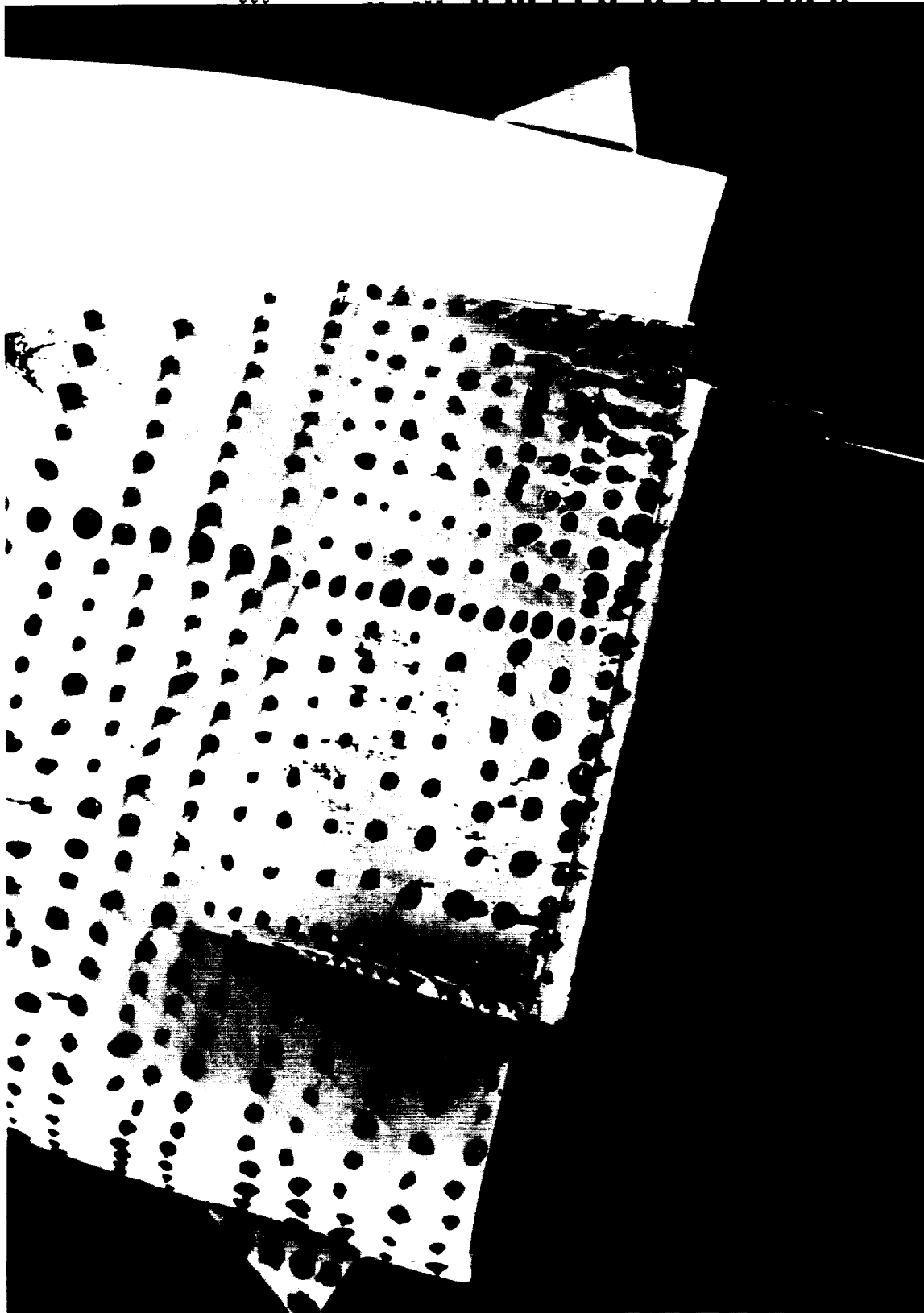
Figure 15.- Concluded.



A-36010

(a) Shock-tunnel model; $M_\infty = 14$, $Re_\infty, \lambda = 0.035 \times 10^6$, $\alpha = 15^\circ$, $\delta_p = 40^\circ$, $\delta_r = 35^\circ$.

Figure 16.- Visualization of the surface flow on the M2-F2 model.



A-36008

(b) Closeup of shock-tunnel model.

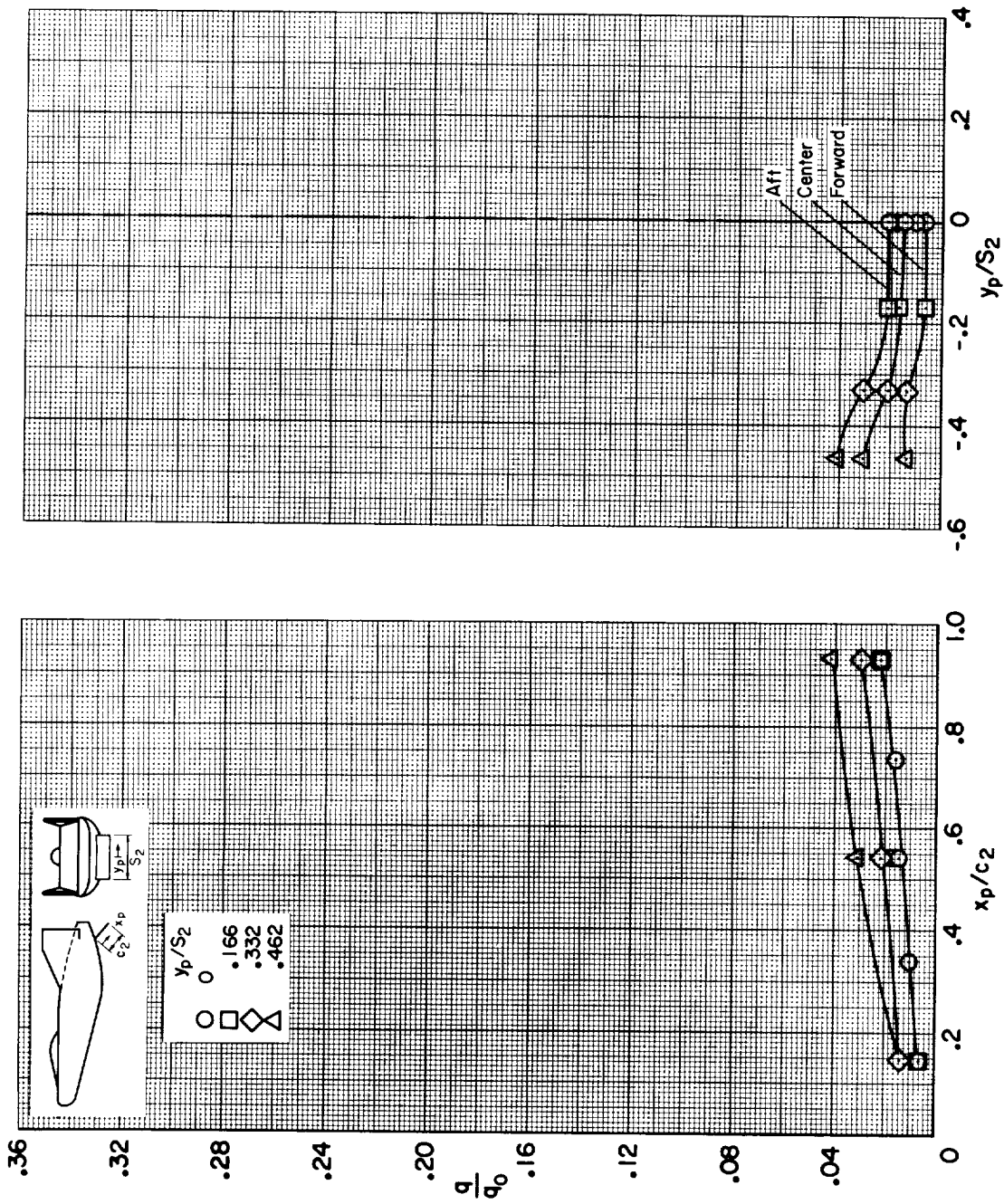
Figure 16.- Continued.



A-36075

(c) 3.5-foot tunnel model; $M_\infty = 10.4$, $Re_\infty, \tau = 0.4 \times 10^6$, $\alpha = 15^\circ$, $\delta_p = 40^\circ$, $\delta_r = 35^\circ$.

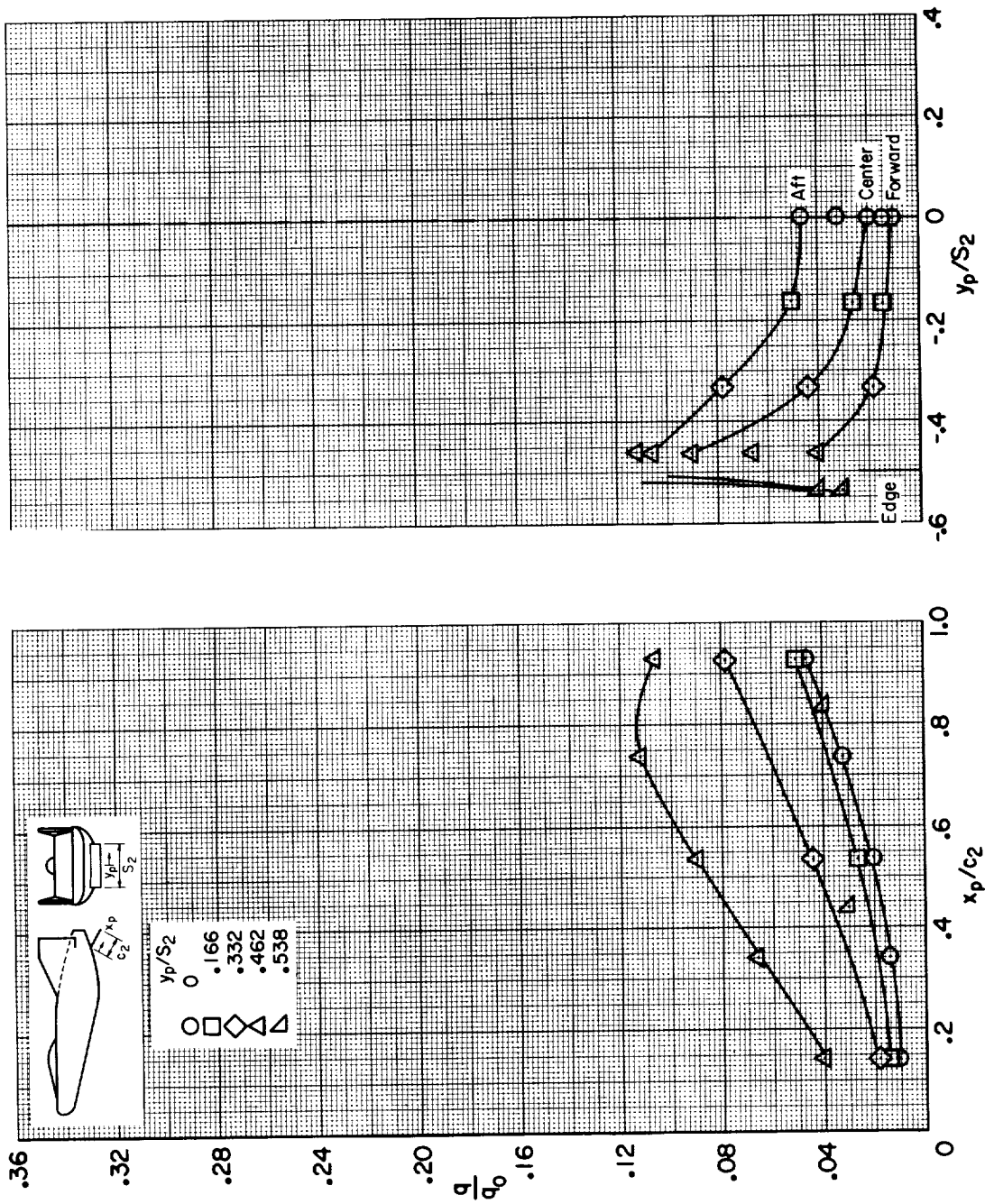
Figure 16.- Concluded.



(a) Longitudinal.

(b) Spanwise.

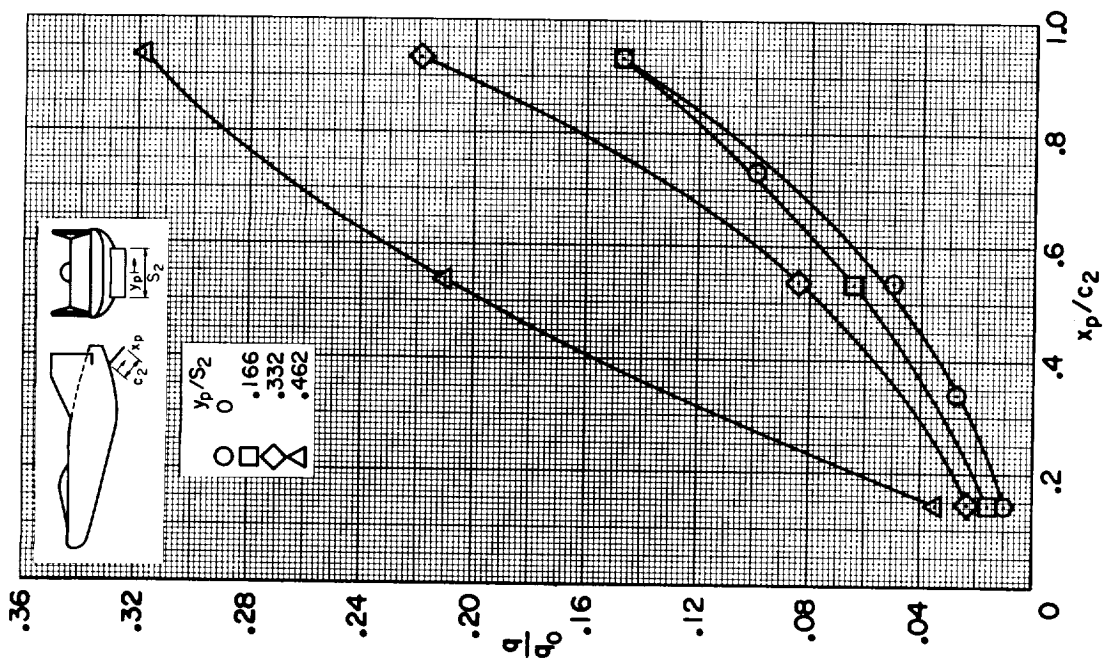
Figure 17.- Heating of the M2-F2 pitch control in the shock-tunnel flow at $M_\infty = 10$; $\alpha = 0^\circ$, $\delta_p = 40^\circ$.



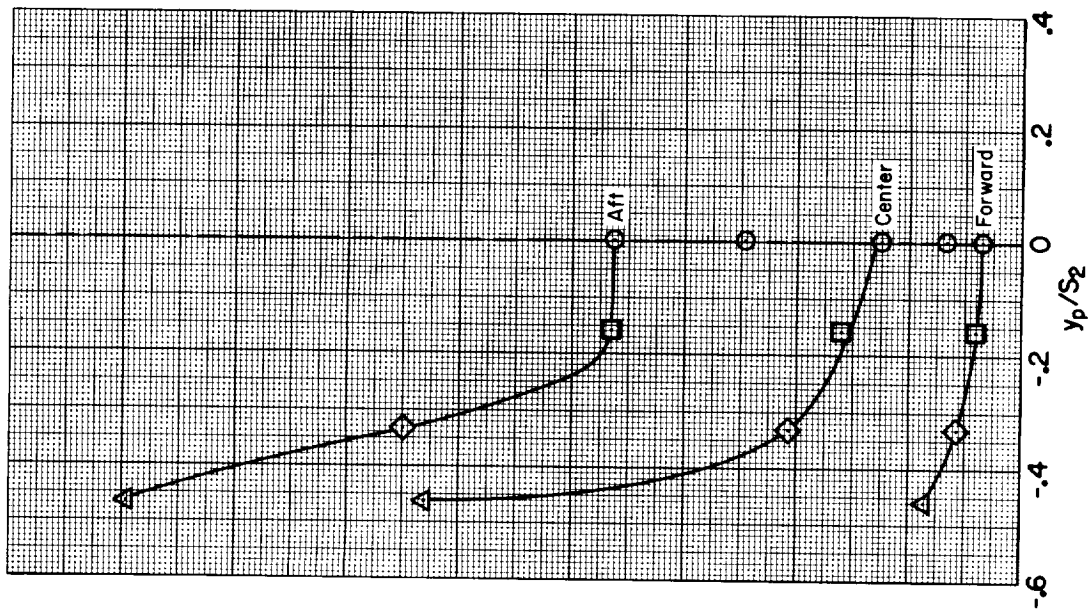
(a) Longitudinal.

(b) Spanwise.

Figure 18.- Heating of the M2-F2 pitch control in the shock-tunnel flow at $M_\infty = 10$; $\alpha = 15^\circ$, $\delta_p = 30^\circ$.

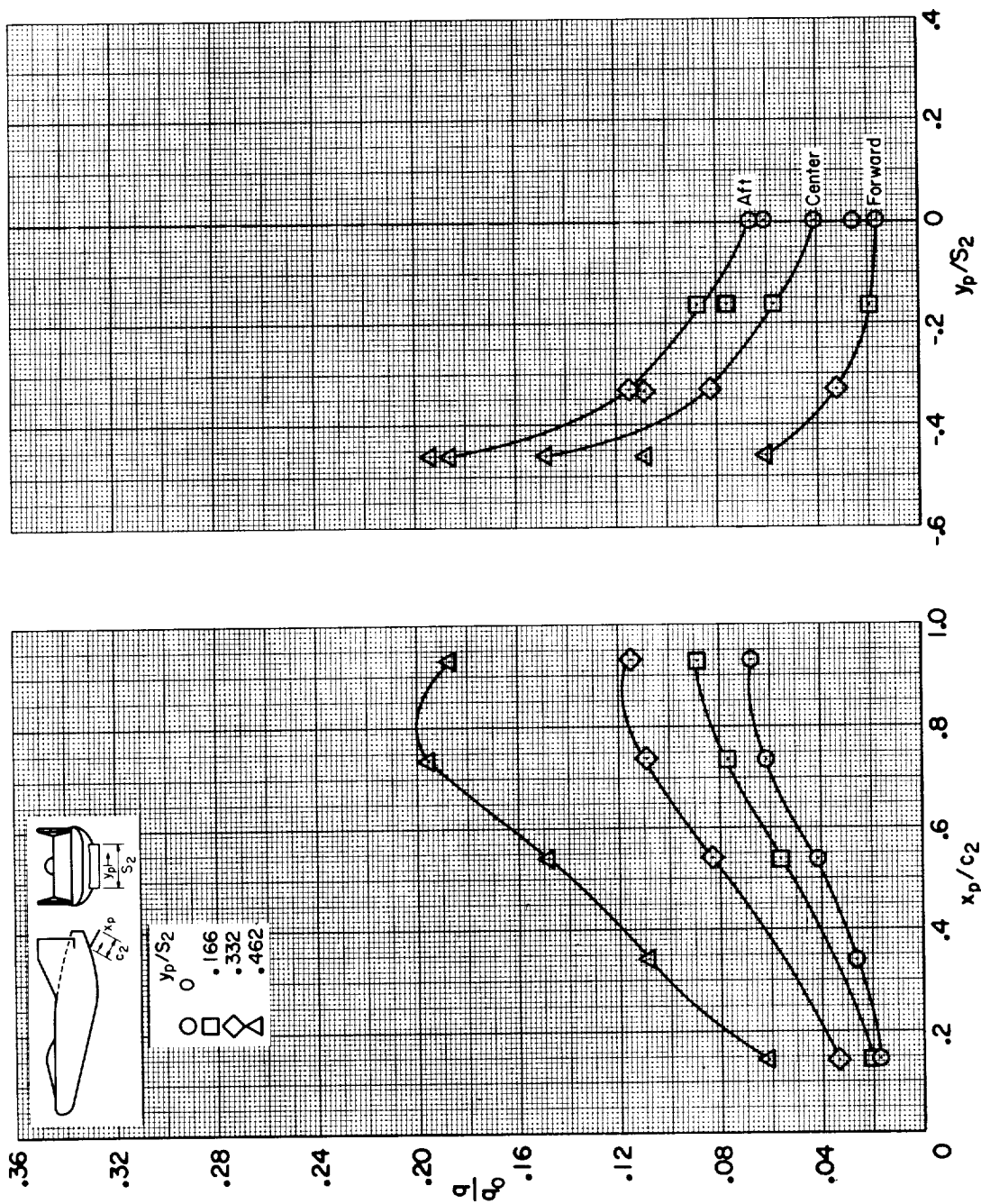


(a) Longitudinal.



(b) Spanwise.

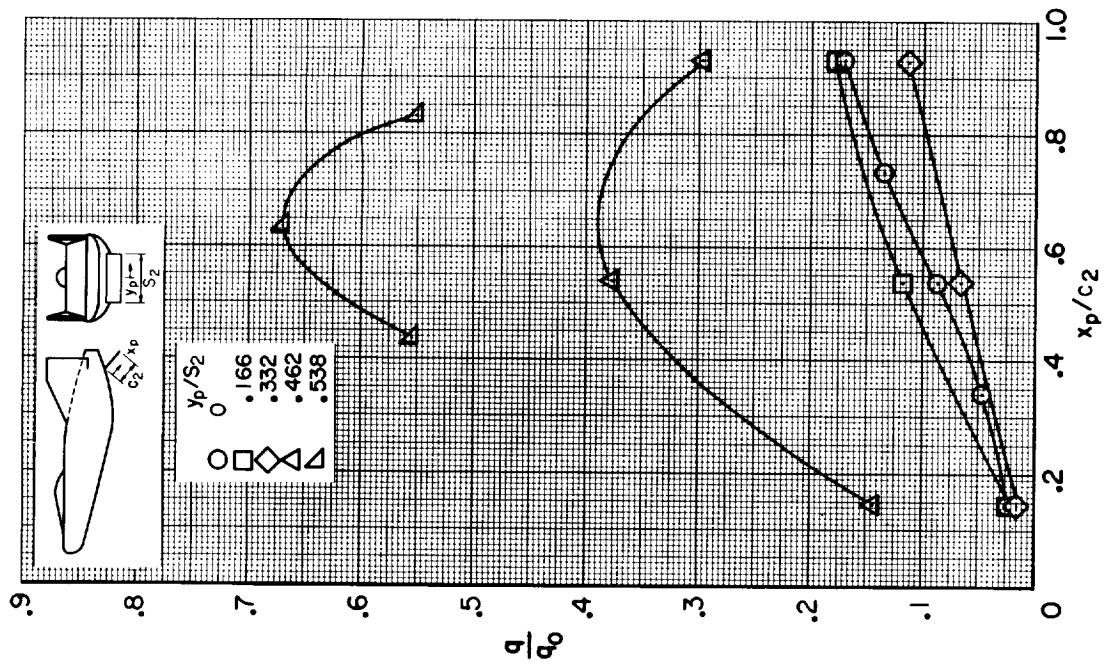
Figure 19.- Heating of the M2-F2 pitch control in the shock-tunnel flow at $M_\infty = 10$; $\alpha = 15^\circ$, $\delta_p = 40^\circ$.



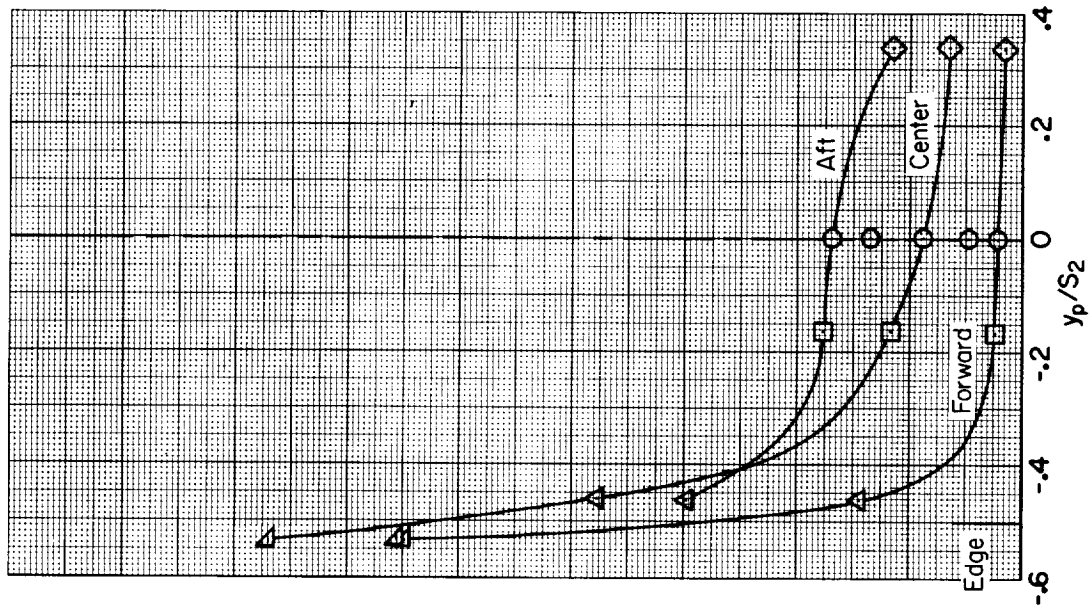
(a) Longitudinal.

(b) Spanwise.

Figure 20.- Heating of the M2-F2 pitch control in the shock-tunnel flow at $M_c = 10$; $\alpha = 20^\circ$, $\delta_p = 30^\circ$.



(a) Longitudinal.



(b) Spanwise.

Figure 21.- Heating of the M2-F2 pitch control in the shock-tunnel flow at $M_\infty = 10$; $\alpha = 15^\circ$, $\beta = 15^\circ$, $\delta_p = 40^\circ$.

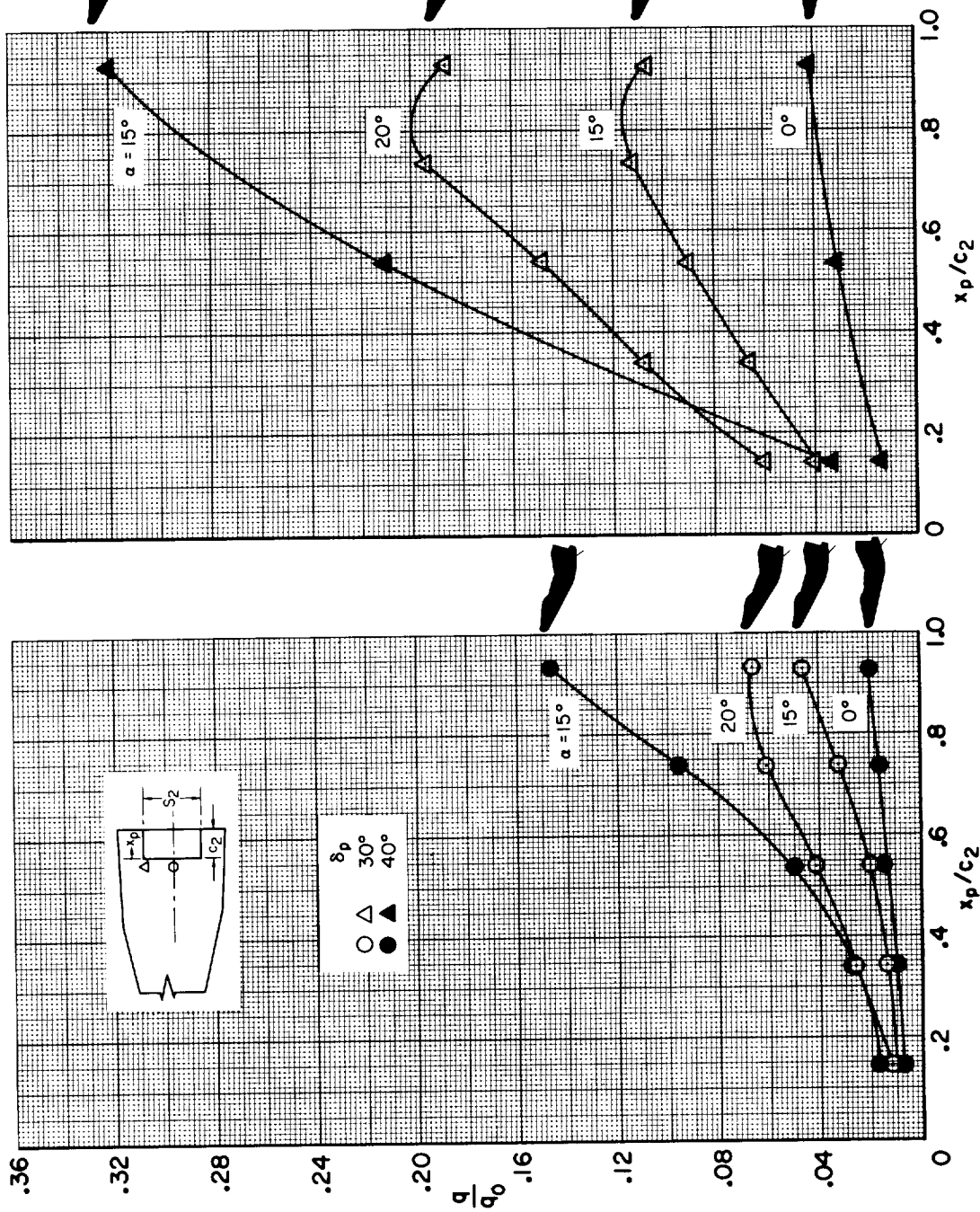


Figure 22.- Heating at the center of the M2-F2 pitch control in the shock-tunnel flow at $M_\infty = 10$.

Figure 23.- Heating at the edge ($y/S_2 = 0.462$) of the M2-F2 pitch control in the shock tunnel flow at $M_\infty = 10$.

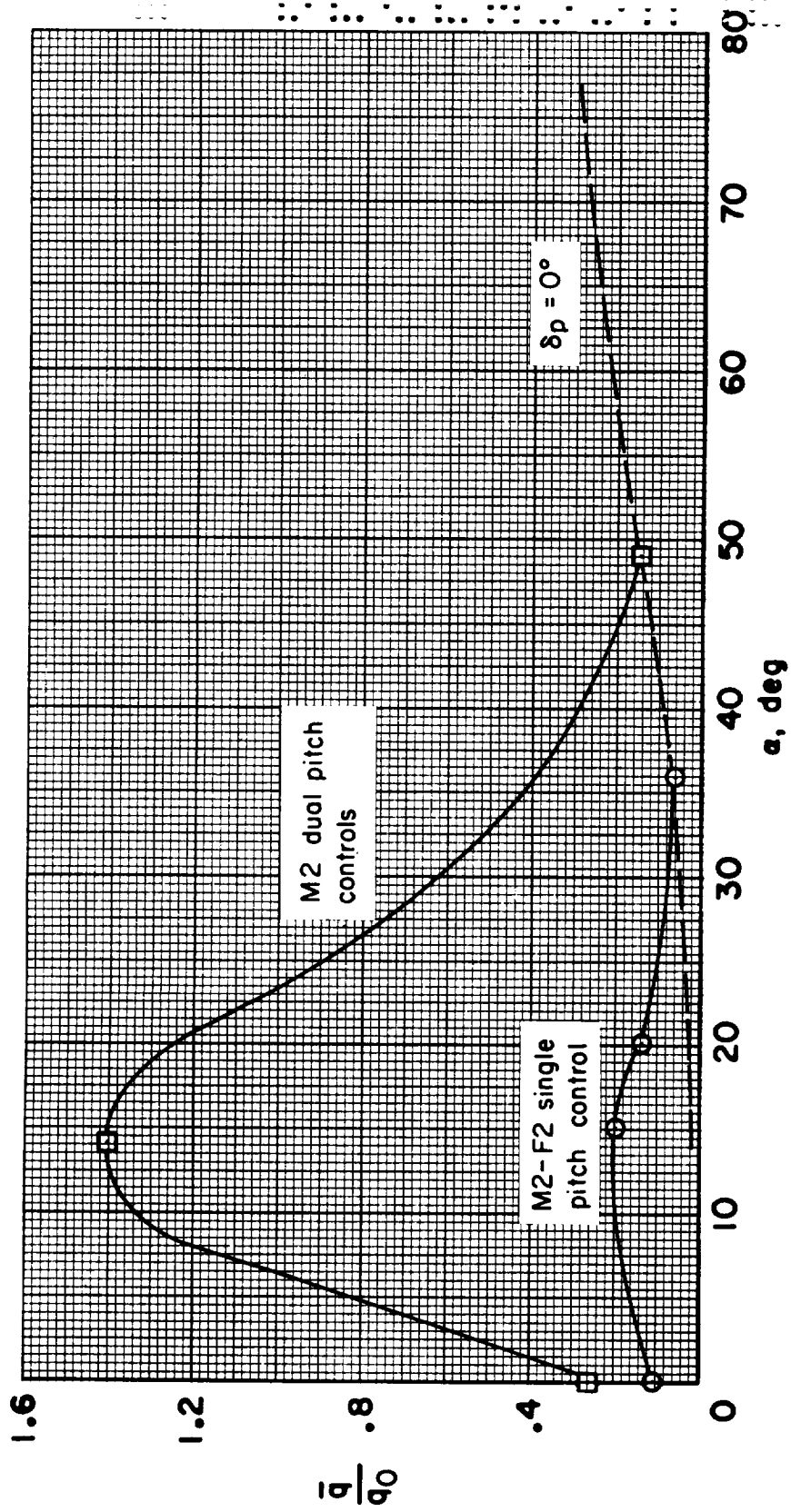


Figure 24.- Comparison of the average heat transfer to the pitch controls of the M2 and M2-F2 at $M_\infty = 10$ in the shock-tunnel flow.



A-30514-1

(a) Side view.

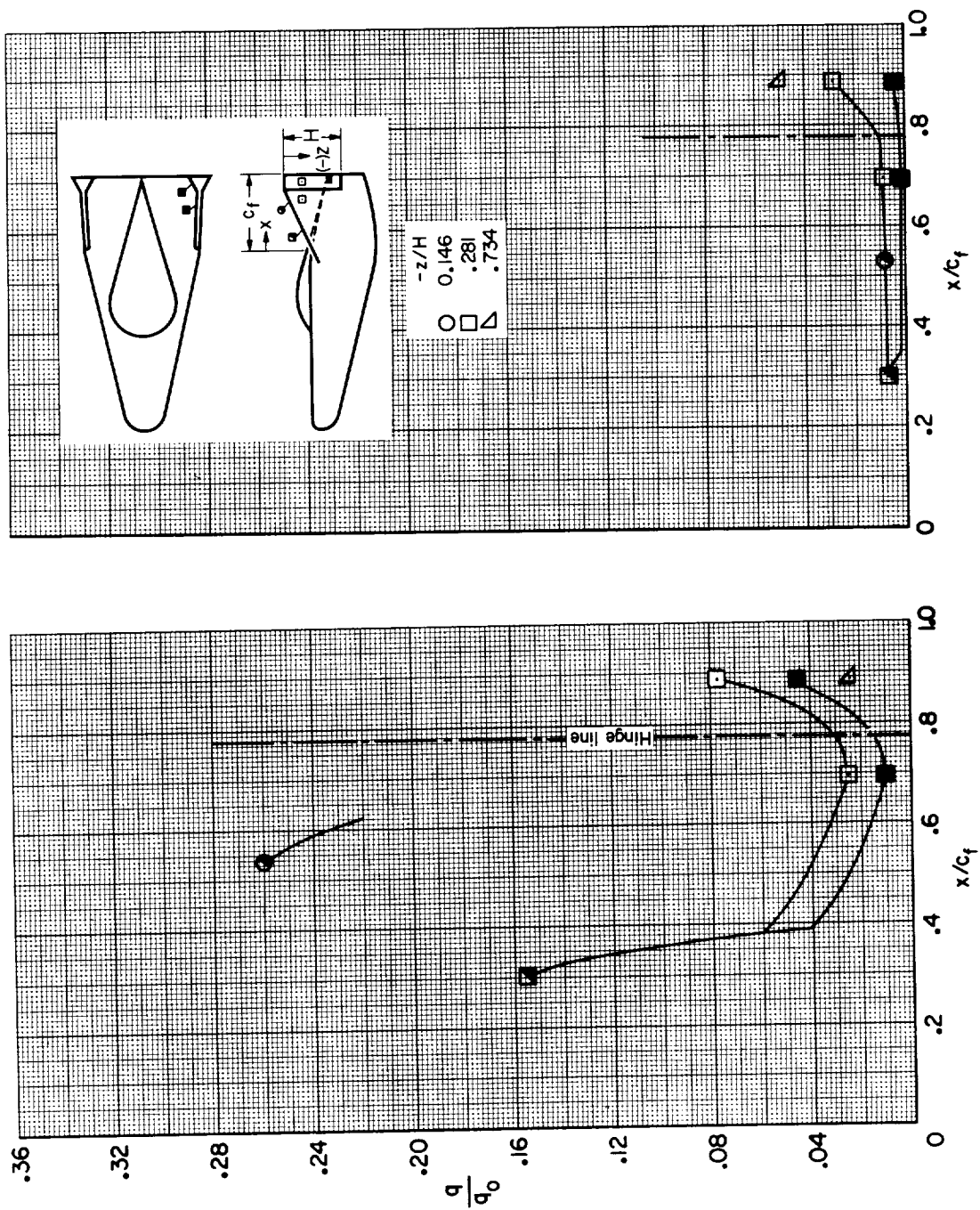
Figure 2b.- Visualization of the surface flow on the M2 model after test in the shock tunnel at $M_\infty = 10$; $\alpha = 0^\circ$, $\delta_r = 35^\circ$.



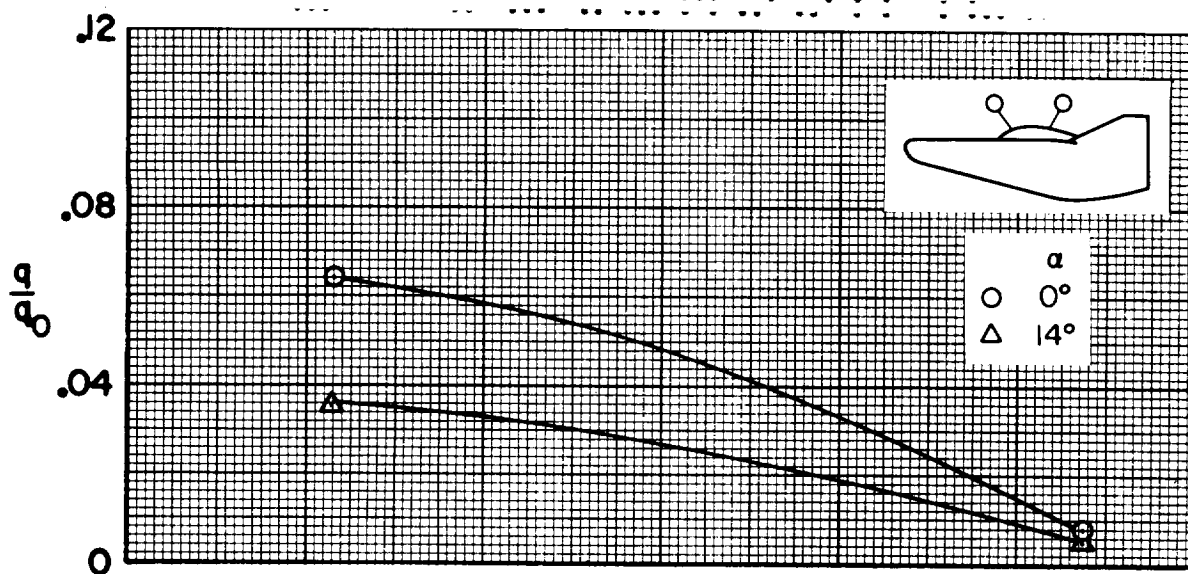
(b) Top view.

Figure 25.- Concluded.

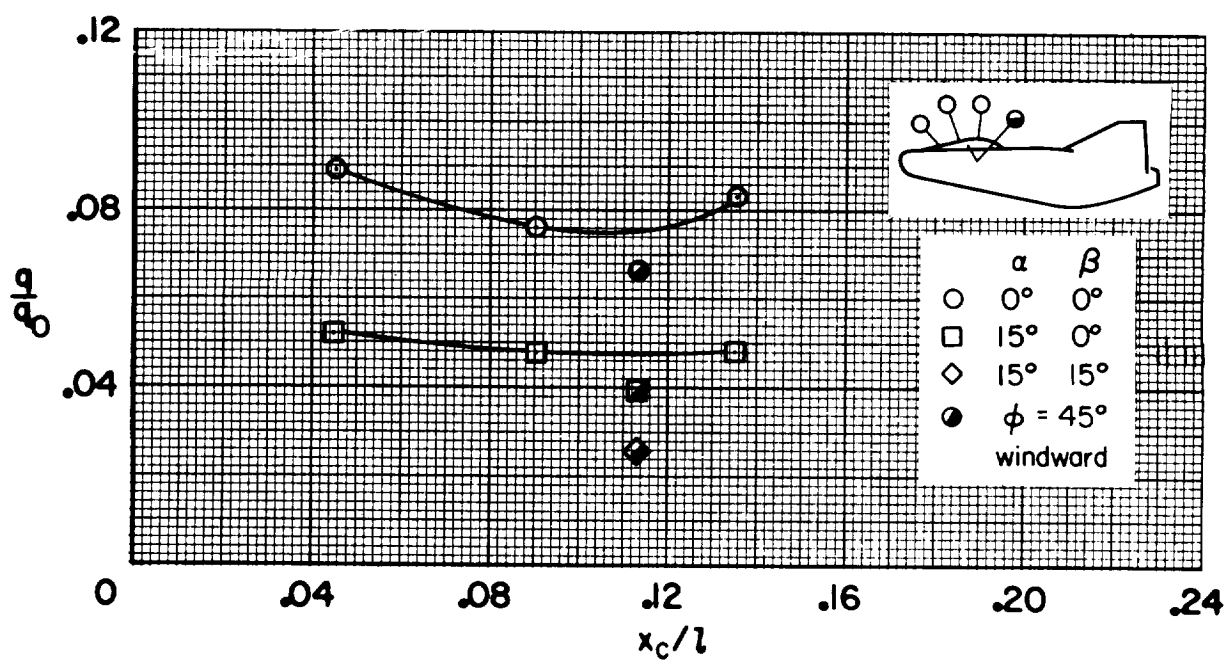
A-30514-3



(a) $\alpha = 0^\circ$, $\delta_r = 35^\circ$
 (b) $\alpha = 14^\circ$, $\delta_r = 35^\circ$
 Figure 26.- Heating of the M2 fin and rudder in the shock-tunnel flow at $M_\infty = 10$.

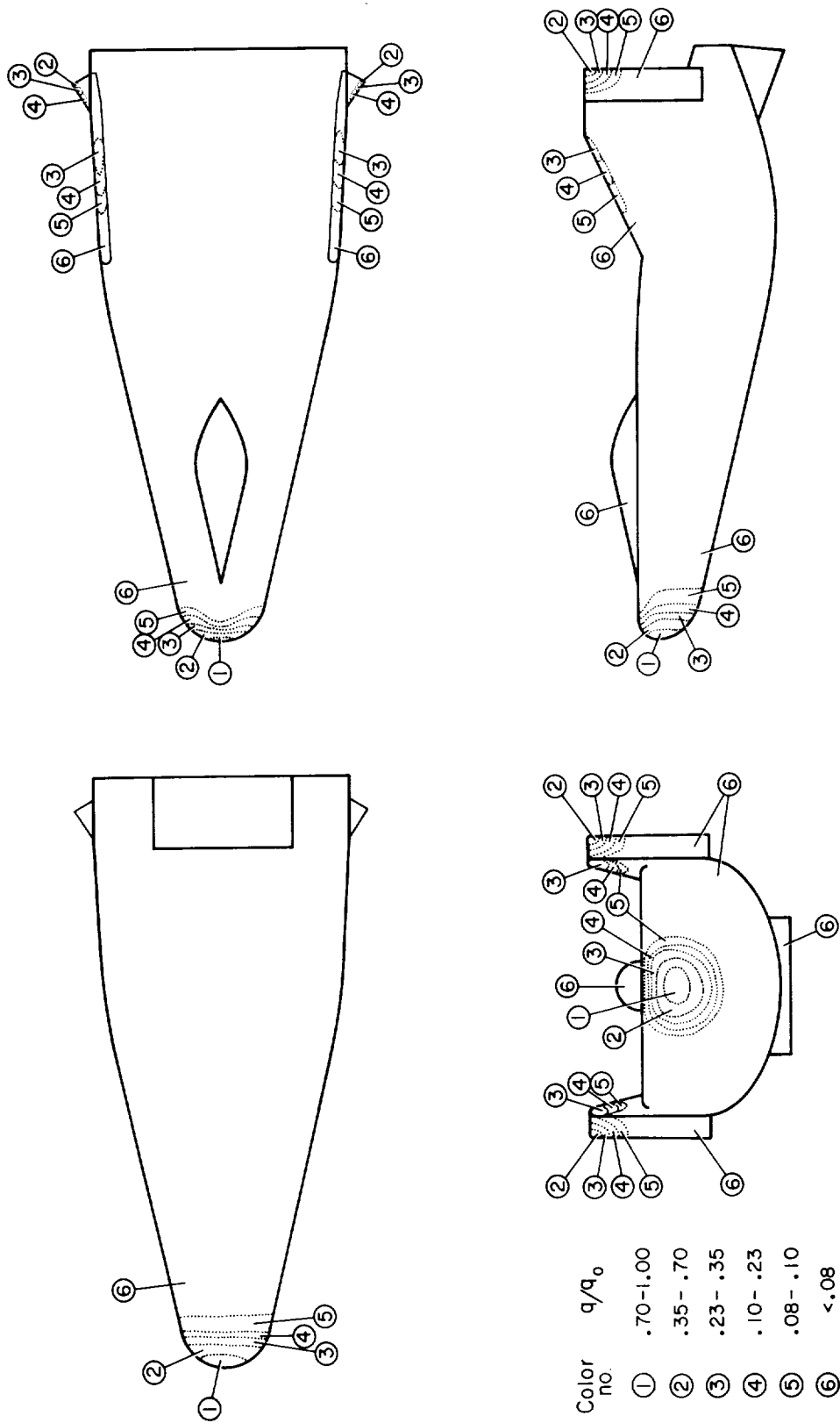


(a) Hemispherical canopy (aft).



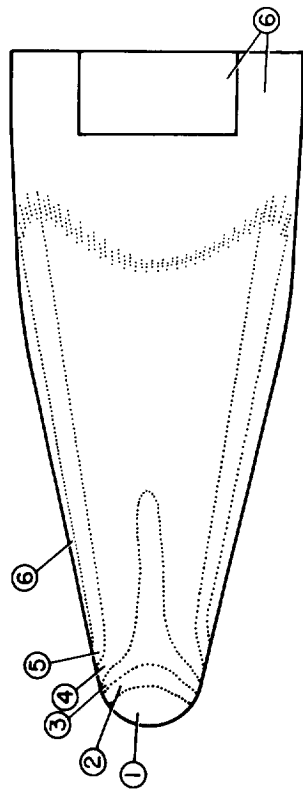
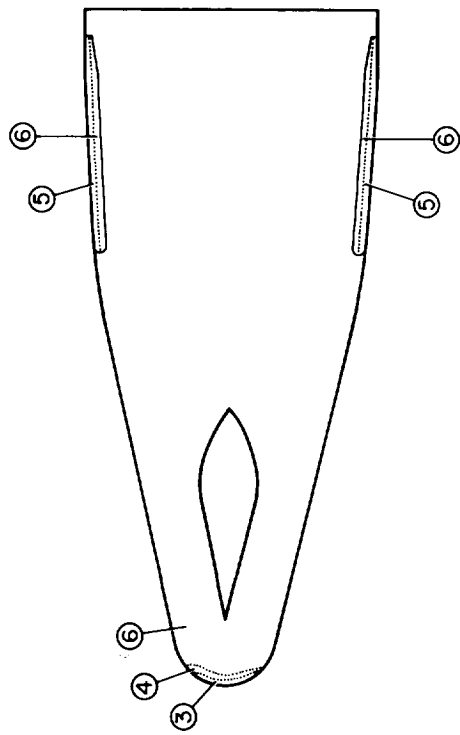
(b) Conical canopy (forward).

Figure 27.- Heating of two canopies in the shock-tunnel flow at $M_\infty = 10$.

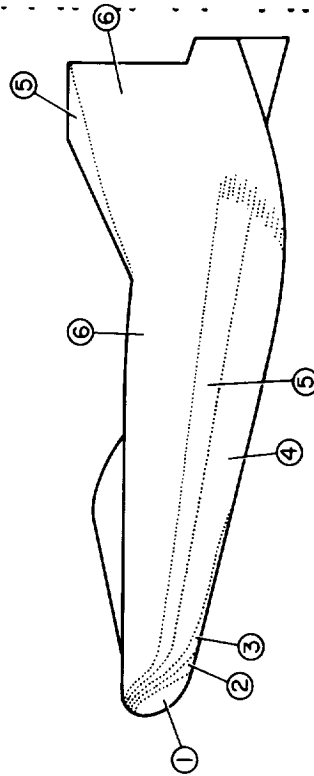
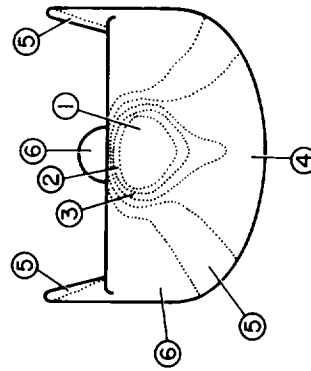


(a) $\alpha = 0^\circ$, $\delta_p = 40^\circ$, $\delta_r = 35^\circ$

Figure 2(a). - Contours of constant heating on the M2-F2 obtained from paint fringe patterns after test in the shock tunnel at $M_\infty = 14$.

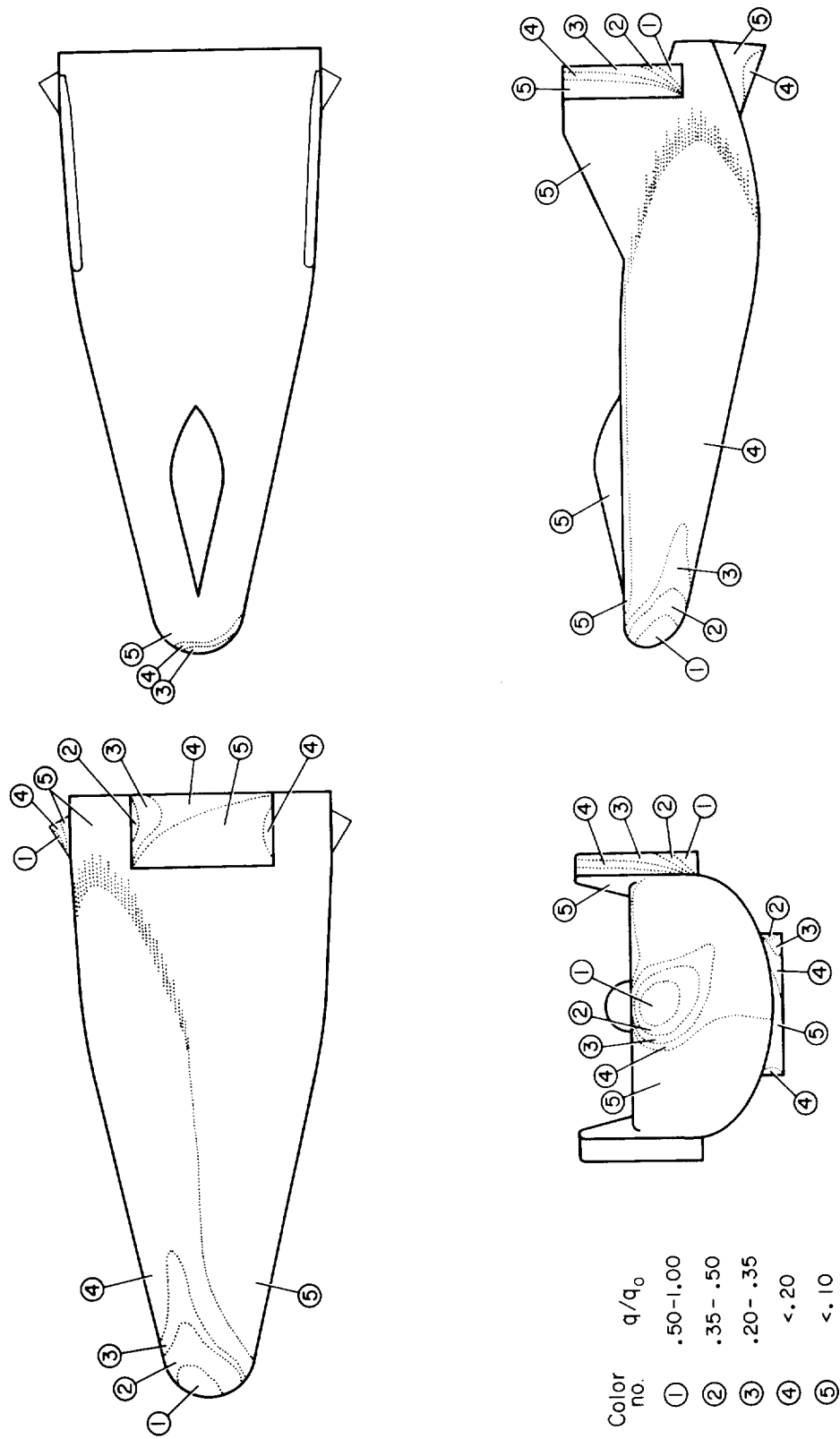


Color no.	q/q_0
①	.52-1.00
②	.32-.52
③	.19-.32
④	.03-.19
⑤	<.03
⑥	<.02



(b) $\alpha = 15^\circ$, $\delta_p = 30^\circ$, $\delta_r = 0^\circ$

Figure 28.- Continued.





(a) Isotherm positions shortly after start of test.

A-40854

Figure 29.- Color-change thermal paint test of the M2-F2 in the 3.9-foot tunnel flow at $M_\infty = 10.4$;
 $\alpha = 17^\circ$, $\delta_p = 0^\circ$, $\delta_r = 0^\circ$.



(b) Midtest appearance.

Figure 29.- Continued.



A-35948

(c) Bottom view of model after test; heating rates: brown $> 0.3 q_0$, blue $= 0.05$ to $0.3 q_0$,
off-white $< 0.05 q_0$.

Figure 29.- Continued.



A-35949

(d) Top view of model after test; heating rates: brown $> 0.3 q_0$, blue = $0.0 q_0$, pink $< 0.0 q_0$.

Figure 29.- Concluded.



(a) Isotherm positions shortly after start of test.

A-40856

Figure 30.- Color-change thermal paint test of the M2-F2 in the 3.5-foot tunnel flow at $M_\infty = 10.4$;
 $\alpha = 30^\circ$, $\delta_p = 15^\circ$, $\delta_r = 25^\circ$.



A-40857

(b) Midtest appearance.

Figure 30.- Continued.



A-36072

(c) Bottom view of model after test. Heating rates: brown $> 0.3 q_0$, blue $= 0.05$ to $0.3 q_0$, pink $< 0.05 q_0$.

Figure 30.- Concluded.



A-35950

Figure 31.- M2-F2 model after thermal paint test in the 3.5-foot tunnel flow at $M_\infty = 10.4$; $\alpha = -7^\circ$, $\delta_r = 25^\circ$. Heating rates: black $> 0.45 q_0$, blue $= 0.06$ to $0.45 q_0$, pink $< 0.06 q_0$.